HAW
HAMBURG

MASTERTHESIS
Lukas Becker

Analysis of Minimal MIMO-SAR Techniques for Human-Machine Collaboration in Industrial Environments

FAKULTÄT TECHNIK UND INFORMATIK
Department Informations- und Elektrotechnik

Faculty of Engineering and Computer Science
Department of Information and Electrical Engineering

HOCHSCHULE FÜR ANGEWANDTE WISSENSCHAFTEN HAMBURG
Hamburg University of Applied Sciences

Lukas Becker

Analysis of Minimal MIMO-SAR Techniques for Human-Machine Collaboration in Industrial Environments

Masterthesis eingereicht im Rahmen der Masterprüfung
im Studiengang Informations- und Kommunikationstechnik
am Department Informations- und Elektrotechnik
der Fakultät Technik und Informatik
der Hochschule für Angewandte Wissenschaften Hamburg

Betreuender Prüfer : Prof. Dr. Jörg Dahlkemper
Zweitgutachter : Dr. Christian Tschoban

Abgegeben am 11. April 2023

Abstract

The need to make robot-human collaboration safer and to extend robot perception in general with all possible sensory interfaces available on the market is rising due to the increased automation of logistic centers and fabrication halls worldwide. Multiple Input Multiple Output Synthetic Aperture Radar (MIMO-SAR) in that context presents a sparsely regarded field of research. It has gained popularity in close range applications due to the availability of low cost highly integrated sensors - especially in the security and medical sector. Previous research evaluated a variety of imaging algorithms and outlined clear limitations. This thesis studies the applicability of MIMO-SAR imaging to robot perception in industrial areas and presents a practical approach and implementation. The range-migration algorithm is used in combination with two radar systems, featuring a state of the art sensor and varying antenna layouts. The imaging results show the correct spatial location of objects with very limited resolution orthogonal to the robots movement direction. This demonstrates that in principle MIMO-SAR may be used as an additional perception vector, even though it has limited usability for close range human-robot collaboration safety. Alternative applications include imaging hidden objects in warehouses or areas not scannable by optical sensors. Complexity arising from non-linear movements of robots may be solved by applying latest advancements in the field.

Der Bedarf nach sicherer Zusammenarbeit von Menschen und Roboter, sowie die Verbesserung von robotischer Wahrnehmung durch Nutzung aller möglichen Sensorschnittstellen im Allgemeinen, steigt durch die zunehmende Automatisierung von Logistikzentren und Fabrikationshallen weltweit. In diesem Kontext ist Multiple Input Multiple Output Synthetic Aperture Radar (MIMO-SAR) ein wenig beachtetes Forschungsfeld. MIMO SAR hat gerade durch die Verfügbarkeit von preisgünstigen und hochintegrierten Sensoren Popularität in Nahbereichsanwendungen gewonnen - vor allem im Sicherheits- und Medizinsektor. Eine große Vielfalt von bildgebenden Algorithmen sowie deren Limitierungen wurden durch bisherige Forschung evaluiert. Diese Thesis untersucht die Anwendbarkeit von bildgebenden MIMO-SAR Verfahren für robotische Wahrnehmung in industriellen Umgebungen und präsentiert eine praktische Herangehensweise sowie Implementierung. Der Range-Migration Algorithmus wird in Kombination mit zwei modernen Radarsystemen mit unterschiedlichen Antennenanordnungen verwendet. Die Abbildungsergebnisse lösen die untersuchten Objekte räumlich korrekt auf, zeigen dabei jedoch sehr begrenzte Auflösung orthogonal zur Bewegungsrichtung. Das demonstriert eine prinzipielle Verwendbarkeit von MIMO-SAR als zusätzliche Möglichkeit der Umgebungserfassung, trotz begrenztem Nutzen für die Verbesserung der Zusammenarbeit von Mensch und Roboter. Alternative Anwendungsgebiete beinhalten die Erfassung von verdeckten Objekten in Warenlagern oder in für optische Sensoren nicht erschließbaren Umgebungen. Die durch nicht lineare Bewegungen entstehende Komlpexität kann durch die Anwendung von aktuellen Fortschritten in dem Forschungsbereich gelöst werden.

The measurement results and various components of the implementation are found on the data storage device attached to the printed version of this thesis.

Contents

Abstract iii

Contents v

1 Introduction 1
- 1.1 Hazards of Human-Robot Collaboration . . . 1
- 1.2 Active and Passive Environmental Sensors . . . 2
  - 1.2.1 Ultrasound and Light Sensors . . . 2
  - 1.2.2 Radar . . . 3
- 1.3 Target System and Development Goal . . . 4

2 Background and State of the Art 7
- 2.1 Frequency-Modulated Continuous Wave Radar . . . 7
- 2.2 Multiple Input Multiple Output . . . 11
- 2.3 Synthetic-Aperture Radar . . . 12
- 2.4 Related Work . . . 13

3 Problem Analysis 15
- 3.1 Feasibility of Radar Application on Robotic Systems . . . 15
- 3.2 Reflectivity Differentiation with Electromagnetic Waves . . . 16
  - 3.2.1 Reflection Loss of Metal Surfaces . . . 17
  - 3.2.2 Reflectivity of Human Tissue . . . 18
  - 3.2.3 Differentiation Based on Material Properties . . . 19
- 3.3 MIMO-SAR Sampling . . . 19
  - 3.3.1 Spatial and Range Resolution . . . 19
  - 3.3.2 Spatial sampling distance . . . 20
- 3.4 Technical Aspects of Floor Logistic Robots . . . 22
  - 3.4.1 Measurement Speed . . . 22
  - 3.4.2 Movement Path . . . 23
  - 3.4.3 Motion Detection . . . 23
- 3.5 Formulated Research Question . . . 23

4 Methods 25
- 4.1 Hardware Selection . . . 25
- 4.2 Algorithmic Basis . . . 27
  - 4.2.1 The Virtual Monostatic Aperture . . . 27
  - 4.2.2 Sampling with a Monostatic Monochromatic Aperture . . . 28
  - 4.2.3 Sampling with a Monostatic Wide-band Aperture . . . 30

4.3 Mathematical Limitations 32
4.4 Summary 33

5 Implementation 35
5.1 Hardware Components 35
5.1.1 DCA1000 Raw Data Capture Board 35
5.1.2 IWR6843ISK Evaluation Board 37
5.1.3 Custom Evaluation Board 38
5.1.4 Custom Board Connectivity Module 38
5.1.5 Linear Rail Motor 40
5.1.6 Targets and Calibration Devices 42
5.2 Software Components 42
5.2.1 MMWave Studio 43
5.2.2 Matlab Imaging Toolbox 43
5.3 Measurement Procedure 44
5.3.1 Device Configuration 44
5.3.2 Movement 45
5.3.3 Post-processing 45
5.3.4 Calibration 46
5.4 Parameter Selection 46
5.4.1 Sensor and Chirp Parameters 47
5.4.2 SAR Parameters 47

6 Results 49
6.1 IWR6843ISK Radar Board 49
6.1.1 Overhead Small Objects Evaluation 49
6.1.2 Ground Level Evaluation 49
6.2 IWR6843 Custom Board 54
6.3 Discussion 56

7 Conclusion 59

Bibliography 61

List of Terms 67

List of Figures

1.1 Caged safety zone around multiple robotic arms in an industrial environment 1

1.2 Phased-array radar sensor used in the automotive sector 4
1.3 Picture of the target robotic system. A phased array radar system is attached to the side of the robot constantly surveying the surroundings. The radar supports established perception system such as cameras and LIDAR sensors. 5
2.1 Classic FMCW signal where the red line indicates the transmitted signal. The frequency is increased until the maximum frequency $f_c + \frac{B}{2}$ is reached and decreased. The blue line indicates the received signal. A shift in the time division indicates the distance to a reflector, the shift in frequency indicates the doppler shift introduced by a moving target 7

2.2 Fast chirp FMCW signal where the black line is the transmitted frequency chirp and the red line is the corresponding received signal. In contrast to the classic chirp the transmission is stopped upon reaching $f_c + \frac{B}{2}$ 8
2.3 Configurable chirp parameters in a TI automotive radar system. 10
2.4 A rotating air surveillance radar using the directivity and therefore the radiated power in different directions to make conclusions about the azimuth of the target. 10
2.5 De-chirping by mixing the received signal with the transmit signal. 10
2.6 Illustration of a planar wave incident on a linear equispaced array. The dotted lines represent the phase fronts of the incident wave. 11

3.1 Transmitted and reflected waves on the surface and inside a conducting material. . . . 17
3.2 Conductivity of human skin based on multiple models dependent on frequency 18
3.3 Permittivity of human skin based on multiple models dependent on frequency 18
3.4 Reflected power of human skin dependent on polarization and angle of incidence based on different models 19
3.5 Propagation path length differences to antennas for different incident angles 21
3.6 Different antenna opening angles influencing the path length differences and therefore the spatial sampling distance 21

4.1 Location of a monostatic virtual antenna derived from a bistatic RX and TX setup . . . 27
4.2 Transformation of an exemplary MIMO array with four RX and 4 TX channels and a resulting 16 virtual monostatic channels. 27
4.3 Monochromatic scanning of a target parallel to the x/y-plane of the SAR aperture . . . 28

4.4 Visualization of different movement possibilities of robots. 1) is a robot moving on a straight path, rotating for every direction change. The antenna aperture is always parallel to the movement direction. 2) is an omnidirectional robot forming a three-dimensional synthetic aperture. 3) is a robot rotating while adhering to a arbitrary path. 33

5.1 The data acquisition over interface is launched over Ethernet (1). The PC configures the DCA1000EVM board and the radar board(2). Further configuration data and the trigger signal is sent to the radar board (3). The captures data is transferred to the DCA1000EVM over the 2-line LVDS interface (4). The PC sends new positioning data to the controller (5) which starts the motor (6). The radar data is afterward processed on the PC(7). . . . 36

5.2 The DCA1000 evaluation module featuring a Lattice FPGA and GBit network interface for capturing ADC data directly over LVDS. 37

5.3 Schematic of the IWR6843 radar sensor. The DSP and MCU are located in the programmable DSP sub-system and Master sub-system. Both can read from the ADC buffer, which stores data from the digital front end. 37

5.4 IWR6843ISK antennas configuration. The RX antennas are marked in blue, whereas the TX antennas are marked in red. Only the first and third TX antennas are used. The resulting virtual antenna array is marked in green. It will either form a equispaced array or a uniform array, depending on the selected sampling distance. $\lambda/4$ forms a uniform array. 38

5.5 The IWR6843ISK module featuring three transmit and four receive antennas connected to a IWR6843 radar sensor. 38

5.7 Custom board antenna configuration. The RX antennas are marked in blue, whereas the TX antennas are marked in red. Every antenna is used, resulting in 12 virtual phase centers. The resulting virtual antenna array is marked in green. A uniform virtual array is formed, if the sampling distance is $\lambda/2$. The distance between the antenna is larger compared to the IWR6843ISK board, resulting in a more sparse virtual array marked in green. 39

5.6 The custom radar module with the IWR6843 radar sensor. The orthogonal antenna rows are visible. The module is mounted on an adapter board for the DCA1000 evaluation module. It also features three TX antennas in the vertical direction and four RX antennas in the horizontal direction 39

5.8 The 3D view of the connectivity module designed in AltiumDesigner. The cutout and solder bridges for the custom board and future designs can be clearly seen. 40

5.9 Two dimensional corner reflector with two rays being reflected back to the sender while having an equally long propagation path inside the reflector 42

5.10 Complex data format for the IWR6843 radar sensor for one chirp recorded by 4 RX channels [75]. 44

6.1 X-Z slice of the scene. From left to right is the convex reflector, the concealed flange bushings and the aluminium cube. (b) shows an overlay of a photo of the actual scene with the objects at the correct positions. 50
6.2 Sampling of the scene in figure 6.3. A human arm was added to the scene between the first two markers. It is visible with its correct extent in X-direction when focusing on the correct range. The arm is no longer visible on image (b) as it is focused 5 cm behind the arm. The flange bushings are still visible, the convex objects ghosts come into view because of its high reflectivity. 50
6.3 Picture of the spatial resolution test with two brass flange bushings concealed in a cardboard box. 50
6.4 The scene features a metal cabinet, a cable drum and a person. The sampled distance is 1000mm. The sampling step is 2.0 mm. All three objects are clearly visible with correct distance from the aperture and size. The metal objects are more reflective and are therefore differentiable to the human tissue. It is worth noting that their cross section is very low in case of the drum handle and cable. 51
6.5 The structures present in the scene are visible in their correct spatial dimensions. Metal objects have a noticeable difference in reflectivity even when behind cover. The attenuation in reflectivity of the plastic box is noteworthy. The two bottom measurements are taken with a sampling distance violating the $\frac{\lambda}{2}$ sampling distance. As predicted ghost targets start to appear resulting from range ambiguities in the range migration algorithm. Apart from this the resolution and correct spatial proportion start to diminish considerably. . 53
6.6 Reflectivity map at 400 mm distance. No objects present can be observed in the image. The images is dominated by strip structures in both the X-direction with a distance of 7.25 mm which is the sampling step distance as well as in the Y-direction. 54
6.7 Range FFT for the custom antenna board. Channel 1 to 4 from top to bottom and left to right. The third transmitter is switched on. A corner reflector was placed at 500 mm in front of the board. The noise floor varies by 20 dB between channels. The corner reflector can be barely seen on channel 3 and 4. The predominant direct cross talk is placed at 100 mm. 55
6.8 The four channels of the ISK antenna board with transmitter number 3 switched on. The cross talk can be observed at 100 mm distance. The corner reflector is visible at 800 mm distance. The noise floor is consistent on all four receiving channels. 55

List of Tables

3.1 Exemplary set of different expected behaviors for targets in robotic environments. . . . 16
3.2 Means of differentiation between targets. 16

5.1 Serial command structure. 41
5.2 Selected parameters for the radar sensor configured in MMWave Studio. 47
5.3 Selected parameters for the stepper motor and SAR setup for the IWR6843ISK board. . 48
5.4 Selected parameters for the stepper motor and SAR setup for the custom board. 48

Introduction 1

1.1 Hazards of Human-Robot Collaboration . 1
1.2 Active and Passive Environmental Sensors 2
1.2.1 Ultrasound and Light Sensors 2
1.2.2 Radar 3
1.3 Target System and Development Goal . . 4

1.1 Hazards of Human-Robot Collaboration

Industrial robots are already dominating the picture of modern factories and production lines. Over 373.000 industrial robots were installed in 2019 alone. They are used to perform a variety of automatable jobs like welding, painting or moving parts. Modern robotic arms are able to lift bulky parts and thus take physical strain off today's factory workers. Robotic platforms are able to independently move multiple tons or quickly deliver goods around a workshop or logistics center [1].

Unlike the climate may suggest, even in the most sophisticated environments, with many repetitive tasks automated, a lot of the existing workforce is not made obsolete. Many typical workers are driven to tasks that require robot and human collaboration [2]. The resulting vicinity and frequent interactions for collaboration makes the historical and massively deployed narrative of robots in cages more and more obsolete [3].

There are various forms of collaboration. They are defined in DIN EN ISO 10218-2 for better selectivity and include Human-Robot-Interaction, Human-Robot-Cooperation and Human-Robot-Coexistence. In the norm they are separated by the level of interaction between man and machine [4]. A higher degree of collaboration and complexity will also generally require greater co-location of human and robot. This will increase the possibility of accidents and unpredicted behaviors [5].

For ensuring safety in collaborative environments, a number of measures are taken, such as intelligent impact force reduction [6], collision avoidance [7] or anticipation of human intent and movement by the robot [8].

[1]: International Federation of Robotics (2020), *IFR Press Conference*

[2]: Dahlin (2019), 'Are Robots Stealing Our Jobs?'

[3]: Cséfalvay (2021), 'As "robots are moving out of the cages" – toward a geography of robotization'

[4]: ISO (2012), *Robots and robotic devices - Safety requirements for industrial robots - Part 2: Robot systems and integration*

[5]: Marvel et al. (2015), 'Characterizing Task-Based Human–Robot Collaboration Safety in Manufacturing'

[6]: Aivaliotis et al. (2019), 'Power and force limiting on industrial robots for human-robot collaboration'

[7]: Vasic et al. (2013), 'Safety Issues in Human-Robot Interactions'

[8]: Huang et al. (2016), 'Anticipatory Robot Control for Efficient Human-Robot Collaboration'

Figure 1.1: Caged safety zone around multiple robotic arms in an industrial environment

All of those procedures require one or more sensory interfaces. Some are directly applied to the robot and work as a skin-like sensor for proximity and pressure sensing [9]. Others monitor the near-field area around a robotic arm by using capacitive antennas mounted to a robotic platform[10]. For the broader application, the most common approach is to oversee the area of a machine, either by sensory interfaces on the machine or installed on the ceiling or walls. Stationary sensors can target many protagonists at the same time and guarantee continuity for the specific zones they monitor. This is implemented in the visible or infrared spectrum by both cameras and LIDARs [11][12]. Apart from that, there are non-stationary sensors that map the surroundings while being mounted to moving robots.

[9]: Pang et al. (2021), 'Review of Robot Skin'

[10]: Lam et al. (2012), 'Collision avoidance of industrial robot arms using an invisible sensitive skin'

[11]: Ebert et al. (2002), 'Safe human-robot-cooperation'

[12]: Taipalus et al. (2011), 'Human detection and tracking with knee-high mobile 2D LIDAR'

Sensory perception does not only form the basis for safe collaboration, it is also direly needed for optimization of paths, general collision avoidance or targeting of objects. Surveillance of work areas by external sensors or other central information systems has always been the key parts of a factory, but today the machines gain autonomy by enhancing sensory data from their point of view.

1.2 Active and Passive Environmental Sensors

Collaboration between human and robot requires creating and enhancing the robot's perception of its environment. A wide variety of techniques is researched, ranging from the basic sensory interfaces to signal processing and classification of the surroundings via machine learning and artificial intelligence. The multitude of sensors to achieve the physical capabilities for cognition are hereinafter reviewed. The sensor systems work both by emitting a signal and recording a form of response (active) or by recording a response stimulated by external energy sources (passive). The focus is set on gaining spatial perception of the environment to detect collaborators and differentiate them from static objects like tools, shelves, walls or materials.

1.2.1 Ultrasound and Light Sensors

Ultrasound perception is predominantly used in medical imaging appliances, such as cancer detection and surgery assistance or nondestructive testing of materials. It works by emitting sound waves above the audible spectrum and recording the reflected signal. Sound travels as longitudinal waves in air and liquids, and also as transversal waves in rigid materials. The waves are modulated by absorption, reflection and transmission factors inside or along material boundaries [13][14]. An issue for e.g. ranging is the slow speed, yet high speed variability of sound in a medium, which slows the acquisition frequency for medium range applications.

Cameras in contrast don't have these limitations. They are often used as passive sensors and do not emit light themselves. Ambient light illuminating surrounding items is reflected into the camera sensor. This makes native ranging by utilizing the propagation speed of light impossible. By comparing pictures either taken on different locations or by two or more cameras at fixed locations, the so-called stereoscopic approach is used to add depth.

Light Detection and Ranging (LIDAR) in comparison senses actively. It is used as a remote sensing method that emits laser beams to create a 3D scan of the surrounding area. It operates in the wave spectrum similar to cameras, but measures propagation time of the light ray. This enables a range approximation using the ray propagation speed. LIDAR sensors are used to track moving people in a shared space by detecting local minima in the range image [15] or combining 2D LIDAR range maps with statistical classification [16]. Often, LIDAR sensors and stereoscopic cameras are combined to gain both accurate range information and use the edge detection opportunities of a visual image. This information can for example be used for intelligent acceleration and deceleration of collaborative robots in the presence of a human actor [17]. Radar is similar to LIDAR, but has a lower resolution due to the smaller wavelength used. Modern integrated systems are however often cheaper.

The advantages of the aforementioned technologies are combined in Time-Of-Flight cameras, which illuminate the scene by emitting a short light pulse themselves. The time the light pulse takes to an object and back is measured and aggregated into a 3D image.

1.2.2 Radar

Radar is an electromagnetic sensor used for detecting, locating, tracking, and recognizing objects of various kinds up to considerable distances. It operates by transmitting electromagnetic energy toward objects, commonly referred to as targets, and observing

[14]: Mathiassen et al. (2016), 'An Ultrasound Robotic System Using the Commercial Robot UR5'

[15]: Scheutz et al. (2004), 'Fast, reliable, adaptive, bimodal people tracking for indoor environments'

[16]: Arras et al. (2007), 'Using Boosted Features for the Detection of People in 2D Range Data'

[17]: Chemweno et al. (2022), 'Innovative safety zoning for collaborative robots utilizing Kinect and LiDAR sensory approaches'

the echoes returned by them [18]. It can thus be used to measure range and velocity of a target, in contrast to conventional cameras, which estimate how far away an object is based on the size of the object in the camera's image amongst other factors.

Both LIDARs and cameras operate in or close to the visible spectrum of electromagnetic waves, so they suffer from varying light conditions, reflective surfaces and absorbent materials such as cloth, plastics and wood. Though some of them illuminate the scene themselves, varying external light sources like hall lighting or sunlight interfere with measurements.
Radar was originally developed during World War II to track enemy aircraft and has been utilized by the maritime industry for decades [19]. The used centimeter or meter wavelengths or the required antenna gain for long range appliances imply a large size antenna or amplifier electronics. Recent advances in semiconductor fabrication are providing the opportunity to build very small and cost-effective single chip integrated radar systems operating at millimeter-wave frequencies and beyond [20]. The higher operational frequencies and wide bandwidths offer better accuracy. A system operating at 76 GHz is able to detect movements that are as small as a millimeter and resolve range differences down to centimeters. This range resolution makes radar viable and interesting for tracking of objects far smaller than ships or airplanes. Today's complementary metal-oxide semiconductor technology allows integration of all radio frequency components, analog-digital-converters, microcontrollers and signal processors into a single chip [21]. Those advancements enable a wide range of possibilities for electromagnetic sensory interfaces and in recent years they have gained significant attention, especially in the medical and automotive sector [22][23]. Radar sensors also tend to be cheaper than industrial cameras or LIDAR systems.

[18]: Skolnik (2022), 'radar'

[19]: Kline (2018), *AIS vs Radar: Vessel Tracking Options*

[20]: Al-Hourani et al. (2018), 'Millimeter-wave integrated radar systems and techniques'

[21]: Iovescu et al. (2020), *The fundamentals of millimeter wave radar sensors*

[22]: Zhao et al. (2015), 'Distance measurement system for smart vehicles'

[23]: Hasch et al. (2012), 'Millimeter-Wave Technology for Automotive Radar Sensors in the 77 GHz Frequency Band'

1.3 Target System and Development Goal

General availability and pricing make it possible to realize large scale applications of radar sensors. This work investigates the feasibility of a radar sensory interface to enhance camera vision and robot perception in general by imaging the reflectivity of the surroundings. Special consideration is given to the ability to differentiate dielectrics such as human skin or plastics from conductive materials such as steel framing or wires in a collaborative robotic

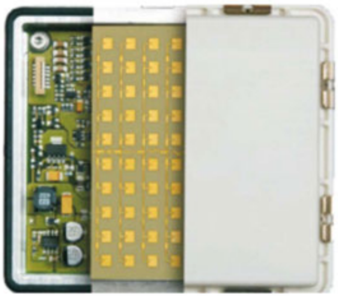

Figure 1.2: Phased-array radar sensor used in the automotive sector

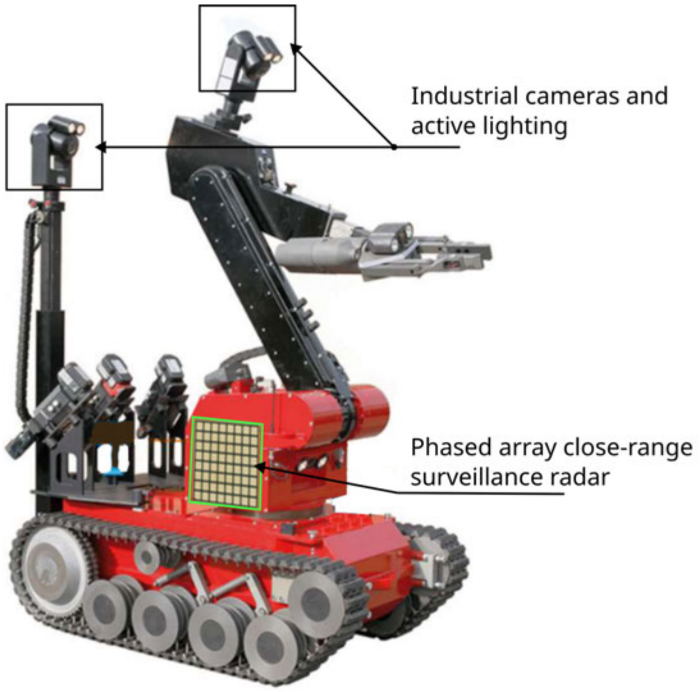

Figure 1.3: Picture of the target robotic system. A phased array radar system is attached to the side of the robot constantly surveying the surroundings. The radar supports established perception system such as cameras and LIDAR sensors.

environment. The use of millimeter wave radar is evaluated against other sensory approaches. A synthetic aperture radar approach for virtually enlarging the aperture of a small and cost-efficient radar sensor by movement along a track is emulated. The system is planned to be attached to a driver-less transport system which is able to navigate autonomously in an industrial environment. The system's capabilities of cooperation are enhanced by a robotic arm. It can lift goods and place them on workbenches and shelves. It can assist workers in assembly and maintenance tasks. This system requires a high quality environment monitoring for pathfinding and navigation. Apart from that, a clear perception of humans as high risk encounters is necessary as close and cautious interaction is needed.

Background and State of the Art 2

2.1 Frequency-Modulated Continuous Wave Radar 7
2.2 Multiple Input Multiple Output 11
2.3 Synthetic-Aperture Radar 12
2.4 Related Work 13

A radar transmits and receives electromagnetic waves, working from a few dozen MHz up to over one hundred gigahertz. It is employed to detect velocity, speed and direction of a target or as an imaging sensor. This makes it similar to cameras and LIDAR, which work with visible or infrared electromagnetic waves. Only a few technologies are viable for the usability of radars in the industrial sector, as it requires close ranges and high range resolution. These key technologies and their current state are hereinafter presented. This shows the possibilities of using radar for the proposed application.

2.1 Frequency-Modulated Continuous Wave Radar

A Frequency-Modulated Continuous Wave (FMCW) radar is transmitting a continuous carrier modulated by a periodic function such as a sinusoidal or sawtooth wave to measure target range per definition of the IEEE [24]. A run-time measurement is performed by comparing the start of the ramp transmission to the easily detectable ramp in the received signal. The time shift (Δt) is the target's range travelled by the radar wave at light speed. The deviation in the frequency at the start of the received ramp is the Doppler shift (Δf), which enables FMCW to simultaneously measure velocity and range (see figure 2.1).

[24]: (2008), 'IEEE Standard Radar Definitions'

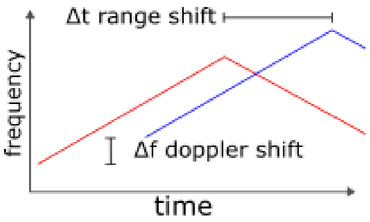

Figure 2.1: Classic FMCW signal where the red line indicates the transmitted signal. The frequency is increased until the maximum frequency $f_c + \frac{B}{2}$ is reached and decreased. The blue line indicates the received signal. A shift in the time division indicates the distance to a reflector, the shift in frequency indicates the doppler shift introduced by a moving target

The frequency ramp by a continuous wave radar is also known as chirp. While for a variety of applications triangular [25][26] or rectangular modulations are used, the fast chirp approach has especially gained utilization prevalence in the automotive and industrial sector. It modulates a rising frequency and shuts off the transmitter upon reaching the highest frequency, like visualized in figure 2.2. It is advantageous due to the increased range resolution without the degradation of velocity resolution compared to the classic FMCW modulation [27]. Additionally, due to the halved duty-cycle, the radar image has both a faster acquisition time and higher Signal-to-Noise Ratio (SNR). Choosing the fast chirp

[25]: Kurt et al. (2008), 'Zero crossing counter for accuracy improvement of FMCW range detection'

[26]: Choi et al. (2022), 'Technique for fast triangular chirp modulation in FMCW PLL'

[27]: Tong et al. (2015), 'Fast chirp FMCW radar in automotive applications'

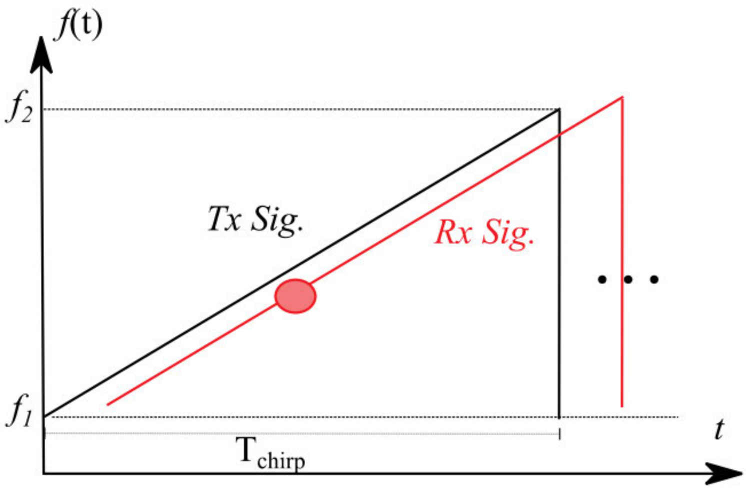

Figure 2.2: Fast chirp FMCW signal where the black line is the transmitted frequency chirp and the red line is the corresponding received signal. In contrast to the classic chirp the transmission is stopped upon reaching $f_c + \frac{B}{2}$

approach seems to be a popular choice at the moment as is offered by most chip manufacturers current in their products. Examples are from Texas Instruments [28], Infineon [29] or NXP [30].

[28]: (2018), *IWR1642 Single-Chip 76- to 81-GHz mmWave Sensor*

[29]: infineon (2022), *XENSIV™ – sensing the world*

[30]: Robertson et al. (2014), *Increasing Automotive Safety Through Embedded Radar Technologies*

[31]: Kumar et al. (2022), *A Compact Quasi-Yagi Antenna for FMCW Radar-on-Chip based Through-Wall Imaging*

The efficiency of these systems can be further improved by dechirping the signal in compact radar sensors. This is directly done in the high frequency section of the receiver (e.g. figure 2.5 [31]). The received signal is mixed with an attenuated copy of the transmitted signal. This attenuation accounts for the expected path loss. Sampling in the baseband of the radar architecture greatly reduces the required sampling frequency dictated by the Nyquist theorem from at least 120 GS/s for a 60 GHz radar to a few MS/s. The sampling frequency depends on the bandwidth, which is defined by the desired range. The reason for this is that the time it takes electromagnetic waves to travel to the maximum range and back, is the time the maximum frequency of the down-converted signa, can shift its phase. This frequency is the upper limit of the bandwidth. This phase-shift must be observed in the fast chirp period, resulting in the minimum sampling frequency. For cost-efficient radar sensors in the industrial and automotive sector, this range is 50 m to 400 m.

When using a fast chirp dechirp-on-receive approach, the transmit frequency for one ramp with bandwidth B and duration $t = [-\frac{T}{2}; \frac{T}{2}]$ starting at the lowest frequency $f_c - \frac{B}{2}$ can be expressed as:

$$f_T(t) = f_c + \frac{B}{T}t \qquad (2.1)$$

The phase $\phi_T(t)$ of the transmitted signal $cos(2\pi f_T(t))$ after integration results in the following equations

$$\phi_T(t) = 2\pi \int f_T(t) - \phi_{T0} dt \tag{2.2}$$

$$\phi_T(t) = 2\pi\left(f_c t + \frac{1}{2} \cdot \frac{B}{T} t^2\right) - \phi_{T0} \tag{2.3}$$

$$\phi_T(t) = 2\pi\left(f_c t + \frac{1}{2} \cdot \frac{B}{T} t^2\right) - \phi_{T0} \tag{2.4}$$

The phase of the signal which is downmixed by the de-chirping process $\Delta_\phi(t) = \phi_T(t) - \phi_T(t - \tau)$ is:

$$\Delta_\phi(t) = 2\pi\left(f_c \tau + \frac{B}{T} t\tau - \frac{B}{2T}\tau^2\right) \tag{2.5}$$

τ is the delay between the transmitted and received signal of one target. The last term in the equation 2.5 can be neglected because $\tau^2/T \ll 1$. A target at the distance R moving in the direction of the receiver with constant velocity v is assumed for the calculation of the delay in term 2.6. This leads to equation 2.7.

$$\tau = \frac{2(R + v \cdot t)}{c} \tag{2.6}$$

$$\Delta_\phi(t) = 2\pi\left[\frac{2 f_c R}{c} + \left(\frac{2 f_c \cdot v}{c} + \frac{2B \cdot R}{T \cdot c}\right) t + \frac{2B \cdot v}{T \cdot c} t^2\right] \tag{2.7}$$

The last term is called Range-Doppler-Coupling and can be neglected again:

$$\Delta_\phi(t) = 2\pi\left[\frac{2 f_c R}{c} + \left(\frac{2 f_c \cdot v}{c} + \frac{2B \cdot R}{T \cdot c}\right) t\right] \tag{2.8}$$

The generated frequency is the derivation of the phase as in equation 2.9. The first of the two terms induces the doppler frequency shift.

$$\frac{d\Delta_\phi(t)}{dt} = \frac{f_{IF}(t)}{2\pi} = \frac{2 f_c \cdot v}{c} + \frac{2B \cdot R}{T \cdot c} \tag{2.9}$$

In practice ranges and velocities are directly extracted from the above Intermediate Frequency (IF) phase by applying one Fast Fourier Transformation (FFT) for the object range and another FFT over multiple range FFTs. This results a range-doppler map containing all targets and their respective velocities [32].

Integrated radar systems enable software configuration of the transmitted chirp. The list below offers an overview of a modern Texas Instrument IWR1642 radar sensor [28][33].

[32]: Meta et al. (2007), 'Signal Processing for FMCW SAR'

[28]: (2018), *IWR1642 Single-Chip 76-to 81-GHz mmWave Sensor*

[33]: (2018), *DCA1000EVM Data Capture Card*

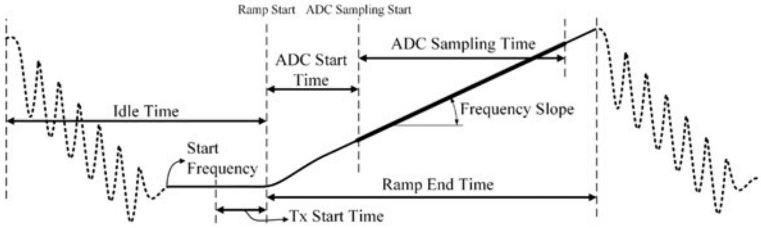

Figure 2.3: Configurable chirp parameters in a TI automotive radar system.

- Start Frequency: The carrier frequency at start
- Frequency Slope: The slope computed by the bandwidth and chirp duration
- Idle Time: Time between end of previous chirp and start of the next
- ADC Start Time: Delay from beginning of the ramp to the start of sampling by the ADC
- TX start time: The time before the start of the ramp when the transmitter turned on
- ADC Sampling Time: The sampling duration of the ADC
- Sampling rate: The ADC sampling rate
- Ramp end time: The point in time to stop the ramp

For detection of multiple moving targets, the combination of one receiver and transmitter is sufficient. Determining the azimuth or elevation of a target with an either bistatic or monostatic pair of antennas is possible by mechanically steering a narrow beam radar over three-dimensional space. Conclusions are made by evaluating the reflected signal strength together with the narrow beam angle of the antenna.

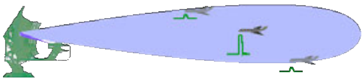

Figure 2.4: A rotating air surveillance radar using the directivity and therefore the radiated power in different directions to make conclusions about the azimuth of the target.

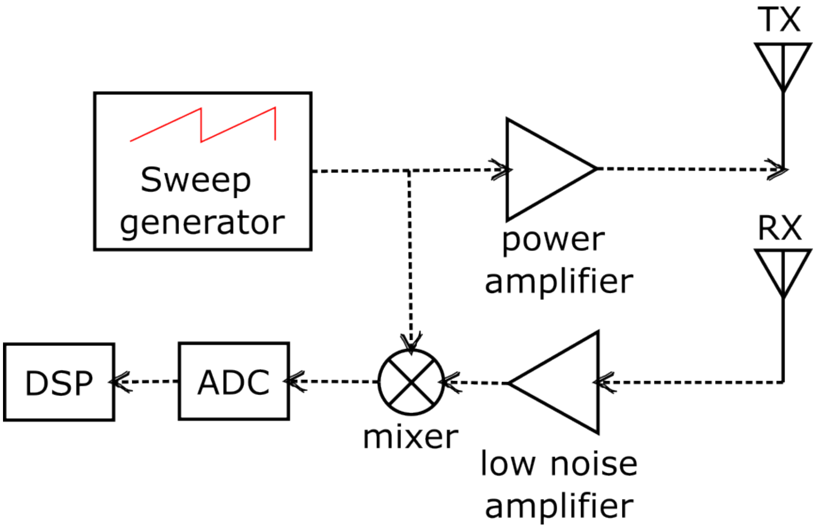

Figure 2.5: De-chirping by mixing the received signal with the transmit signal.

2.2 Multiple Input Multiple Output

As mentioned above, multiple antennas or multiple observation points are needed to gain information about the location of a target. This can be achieved by aggregating multiple receiving and transmitting antennas into one radar aperture. The resulting multi-static radar is known as Multiple Input Multiple Output (MIMO) radar. In contrast to bistatic antenna configurations known as Single Input Single Output (SISO). MIMO radar is characterized by using multiple antennas to simultaneously transmit diverse (possibly linearly independent) waveforms and by utilizing multiple antennas to receive the reflected signals [34]. Systems with multiple antennas can be distinguished by the degree of spatial separation. Distributing antennas throughout a large surveillance area in coherent and non-coherent configurations is a possible setup which Qian He et al. evaluated in [35]. For widely separated antennas, a great benefit comes from being able to mitigate varying RCS of targets by illuminating them from different angles. It is therefore widely used in large area air surveillance radars like reviewed in [36]. In contrast to that, receiving and or transmitting antennas can be placed close to each other in the form of a phased array. The spatial and Doppler resolution is increased compared to a monostatic radar. In [37] Cassidy et al. developed a high resolution range imaging system by employing two integrated MIMO radars. Igal Bilik et. al and others research the use of large MIMO radars for extending automotive visibility in the wake of autonomous cars with azimuth and elevation resolution up to two degrees [38]. Advancements in Complementary Metal-Oxide-Semiconductor (CMOS) technology make highly integrated MIMO sensors possible, featuring not only the VCO and ADC for transmitting and de-chirping radar signals but also DSP's and hardware acceleration modules with enough computing power to extract target locations and speed directly over digital interfaces. However only a few products reached market readiness yet, for example the Texas Instruments sensor fleet.

[34]: Li et al. (2009), *MIMO radar signal processing*

[35]: He et al. (2014), 'Chapter 13 - MIMO Radar with Widely Separated Antennas—From Concepts to Designs'

[36]: Sruti et al. (2021), 'Non-Parametric and Geometric Multi-Target Data Association for Distributed MIMO Radars'

[37]: Cassidy et al. (2022), 'High resolution automotive imaging using MIMO radar and Doppler beam sharpening'

[38]: Bilik et al. (2016), 'Automotive MIMO radar for urban environments'

In the case of multiple transmitter elements, the signal is either transmitted by all antennas simultaneously or one after another and then received by all receiver elements. The reflected wave can often be assumed to be a planar wave for targets in the far-field of the antenna. This greatly reduces the computational effort, especially for large antenna array systems.

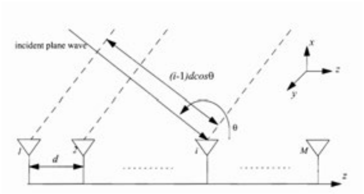

Figure 2.6: Illustration of a planar wave incident on a linear equispaced array. The dotted lines represent the phase fronts of the incident wave.

As shown in 2.6 the incident planar wave, received by an array of receiver antennas, travels longer to the second element than to the first. This offset is described by $dcos(\phi)$ or in terms of phase offset is written by $\zeta_1 = \beta dcos(\phi)$ where β is the phase propagation factor given by $2\pi/\lambda$. Carried over to multiple receiving elements, every next element can be described as $\beta 2dcos(\Phi)$, $\beta 3dcos(\Phi)$ and so on. This clear selectivity gives MIMO arrays the possibility to not only differentiate between range and velocities of target, but also the elevation and azimuth of multiple targets in their view [39].

[39]: Rias (1996), 'Direction of arrival using antenna arrays'

2.3 Synthetic-Aperture Radar

Employing MIMO systems physically enlarges the sensor's size and thus its spatial resolution with up to $N_{RX} \cdot N_{TX}$ different virtual antennas. Especially MIMO arrays with close antenna spacing get very expensive and complex by enlarging and can only illuminate objects in their antenna opening angle. If the surveyed space is too large to construct a MIMO array with the capability to adequately illuminate it or if the radar system is attached to a moving object, several radar measurements can be added together. This creates a virtually larger aperture. It is also beneficial to suppress range and azimuth ambiguities which may occur in a single radar image. This technique is called Synthetic Aperture Radar (SAR) and while not being limited to MIMO apertures, it is often combined in imaging scenarios. For satellite surveillance, multiple real aperture images are integrated along the satellite's one-dimensional trajectory to create images from coherent radar waves [40]. Other applications such as non-destructive testing [41] or concealed item detection [42] move the sensor along a two-dimensional plane in front of an object.

[40]: Kirscht et al. (1998), '3D Reconstruction of Buildings and Vegetation from Synthetic Aperture Radar (SAR) Images'

[41]: Buhari et al. (2019), 'Microwave-Based SAR Technique for Pipeline Inspection Using Autofocus Range-Doppler Algorithm'

[42]: Yanik et al. (2019), 'Near-Field 2-D SAR Imaging by Millimeter-Wave Radar for Concealed Item Detection'

SAR is nearly exclusively used as imaging radar. Analogous to a camera, it projects the energy reflected from the target onto a two-dimensional or three-dimensional image where each pixel represents a radar back-scatter. In comparison with stationary beam-scanning radar, SAR offers finer spatial resolution which depends on bandwidth, center frequency and spatial sampling distance.

Several algorithms are used in SAR imaging today and are often combined with MIMO systems. Based on the standard ranging applications, the Range-Doppler algorithm referenced in chapter 2.1 is used for SAR imaging such as [43] or [44].

[43]: Clemente et al. (2010), 'Fractional Range Doppler Algorithm for SAR imaging'

[44]: Charvat et al. (2012), 'The MIT IAP radar course: Build a small radar system capable of sensing range, Doppler, and synthetic aperture (SAR) imaging'

The range-migration algorithm was originally developed for acoustic imaging by [45]. Today it is widely used for electromagnetic waves in near field applications as it does not rely on far field approximations. Many improvements to this algorithm have been made, Sheen et al. extended it to broadband radar [46] and Yanik et al. introduced sparse sampling to it [47] to reduce the computing effort needed for a fully sampled target. Further research by groups in the field of body scanners is detailed below. Gao et al. [48] researched the effects of multiple SISO and MIMO array topologies and algorithms, concluding that the latter can achieve similar resolutions while featuring a lower number of transceivers in a SAR approach. Further findings include the relatively low additional signal processing needed to enhance the range-migration algorithm by employing equivalent phase center approaches for co-located transmitter-receiver pairs.

[45]: Boyer et al. (1971), 'Reconstruction of Ultrasonic Images by Backward Propagation'

[46]: Sheen et al. (2001), 'Three-dimensional millimeter-wave imaging for concealed weapon detection'

[47]: Yanik (2020), 'MILLIMETER-WAVE IMAGING USING MIMO-SAR TECHNIQUES'

[48]: Gao et al. (2018), 'Novel Efficient 3D Short-Range Imaging Algorithms for a Scanning 1D-MIMO Array'

Algorithms for SAR also differ in terms of the resulting synthetic antenna array. Yanik et al. [47] and Gao et al. [48] interpolate only in the range domain by forming uniform virtual arrays and subsequently interpolating the wave curvature with methods like the Stolt interpolation [49]. Wang et al. in contrast proposes two different algorithms for generic planar arrays, finding that non-uniform FFTs, which are applicable to the problem, have great efficiency for dense MIMO arrays [50].

[47]: Yanik (2020), 'MILLIMETER-WAVE IMAGING USING MIMO-SAR TECHNIQUES'

[48]: Gao et al. (2018), 'Novel Efficient 3D Short-Range Imaging Algorithms for a Scanning 1D-MIMO Array'

[49]: Li (1992), 'Algoritthms For The Implementation Of STOLT Interpolation In SAR Processing'

[50]: Wang et al. (2020), '3-D Short-Range Imaging With Irregular MIMO Arrays Using NUFFT-Based Range Migration Algorithm'

J. W. Smith et al. recently published a novel algorithm for irregular scanning apertures by projecting the recorded data onto a virtual planar monostatic array. While his approach is demonstrated to be robust, it also severely lowers computational complexity in comparison to existing techniques [51].

[51]: Smith et al. (2022), 'Efficient 3-D Near-Field MIMO-SAR Imaging for Irregular Scanning Geometries'

2.4 Related Work

The idea of enhancing robot vision in industrial settings with SAR seems to be rather new. Radar imaging devices attached to robots are used with a robot arm as the aperture forming actuator [52], for automatic pipe inspection robots for non-metallic tube materials [53] or as a position correction system [54]. Apart from that, ground penetrating radar is used to detect buried objects, which in – combination with robots – is used for mine detection

[52]: Watts et al. (2016), '2D and 3D millimeter-wave synthetic aperture radar imaging on a PR2 platform'

[53]: Carrigan et al. (2019), 'Non-destructive Testing of Nonmetallic Pipelines Using Microwave Reflectometry on an In-Line Inspection Robot'

[54]: Ali et al. (2014), 'A Rotating Synthetic Aperture Radar Imaging Concept for Robot Navigation'

as it does not require humans to work in the mortal dangers of a minefield [55][56]. Applications are not limited to land based robots, for example the use of robotic submarines for naval search and rescue missions is currently researched by Cai et al. [57].

Limitations of MIMO SAR imaging are thoroughly laid out in the aforementioned publications. The challenges concerning aperture forming robots are discussed in the research presented in section 2.4. The following chapter will analyze the applicability of radar to the proposed system and the constraints when using MIMO SAR in this context.

[55]: Yektakhah et al. (2019), 'High Resolution Subsurface 3D SAR Imaging Using Robotic Bi-Static Transceivers'

[56]: Williams et al. (2012), 'Autonomous robotic ground penetrating radar surveys of ice sheets; Using machine learning to identify hidden crevasses'

[57]: Cai et al. (2023), 'A Multi-Robot Coverage Path Planning Method for Maritime Search and Rescue Using Multiple AUVs'

Problem Analysis 3

As detailed in chapter 1, the fusion of a diverse field of sensor techniques greatly improves a robot's perception. Radar sensors are predominantly advertised as rangefinders and velocity detectors. It is elaborated in chapter 2 that radar has made huge advancement in the recent years. Especially in it's imaging capabilities, miniaturization and cost-effectiveness. The following chapter lays out the challenges encountered when integrating an off-the-shelf radar sensor into a robotic platform to support other perception systems in identifying and mapping the environment. First, the possible sensory problems in different situations are analyzed. Aspects such as environment conditions, monitored target characteristics and possible encounters of objects and subject in an industrial environment are compared. After that, the electromagnetic basis for reflectivity as the imaging factor is discussed. Finally, the challenges of a moving continuous radar imaging system are laid out. This problem analysis provides the foundation for selecting the methods used in the remainder of this work.

3.1 Feasibility of Radar Application on Robotic Systems

Environment surveillance for the automation of processes needs to detect targets in general, track their speed and distance and their angle to the sensor. Radar in the automotive sector treats every detected target equally to protect driver and car. In contrast, the collaborative environments of an industrial robots requires a more diverse set of behaviors. Table 3.1 offers an exemplary set to visualize the implications of situations a robot may encounter.

Although table 3.1 is not exhaustive, it shows, that context and target type matter for correct behavior of the robot. For example, while people entering the work area of a robot present the same target type, they may have widely varying intentions, depending on context. But also, while a robot and a person transporting goods are working in the same context, they present differing target types and need to be treated with a different level of caution. This is reflected in both work safety standards and certifications of robot

Table 3.1: Exemplary set of different expected behaviors for targets in robotic environments.

Target	Incident	Expected behaviour
Human	Target enters working area of robot	Stop the robot, wait until target has left the area
Human	Target enters working area of robot for a collaborative tasks	Stop the robot until target is ready for collaboration
Robot	Second robot overlaps with working area	Track movement until evasive maneuvers
Material	Material moves inside working area	Pick up material for task
Material	Material moves by the robot	Track target until evasive maneuvers
Environment	Static parts of the environment are present in the working area	Either permanently track or learn location of static parts in the working area

Table 3.2: Means of differentiation between targets.

Information	Technology
Shape of Target	Camera or imaging radar
Material reflectivity	Imaging radar
Material Color	Camera
Meta-Information about objects	Passive information exchange via e.g. NFC or radar tags
Behaviour	Radar or Camera with e.g. Neural Networks
Distance and velocity	Multiple cameras, LiDAR or Radar

safety. Therefore, the ability to differentiate between those factors is clearly important.

Table 3.2 presents possible means of differentiation between objects. Multiple uses for radar technology are suggested, especially where obvious approaches with cameras are not feasible for reasons of light conditions, non-penetrable materials such as cardboard or necessity of velocity measurements.

3.2 Reflectivity Differentiation with Electromagnetic Waves

The property of surrounding objects discernible by radar is their electromagnetic reflectivity. Most antennas used for compact radar sensors are patch antennas, which are often $\lambda/2$ or $\lambda/4$ in size. They are therefore electromagnetically short antennas, for which the far field distance border is at $r >> \lambda$, where r is the distance of an object from the antenna. For many of the following calculations it is thus valid to assume planar waves. At his point it is important to note that in certain scenarios and perspectives this approximation may not hold. Such may be the consideration of a complete wave front over a large portion of the antenna opening angle or areas close to the aperture. [58].

[58]: Rappaport (2002), *Wireless Communications - Principles and Practice*

3.2.1 Reflection Loss of Metal Surfaces

To assess the feasibility of using the electromagnetic reflectivity of objects as an extension to e.g. cameras, the characteristics which effect the reflected power of an object must be considered. As the first step, conducting materials are evaluated. The amount of reflected power by conducting materials is calculated under two assumptions. The first assumption is, that the skin depth σ resulting from the skin effect, is far lower than the material thickness. The skin effect describes the effect that alternating current inside a conductor will decrease in density the further it is away from the surface. The skin depth therefore is the equivalent thickness of a conductor passed through by a direct current with the equal power density. Under this assumption, the attenuation of waves travelling through the medium is so high that the reflection at the next material-material interface is close to 0. This means that the field is only reflected at the surface of the material. The definition 3.1 holds true for frequencies much below $f = 1/(\rho\epsilon)$. The symbol ρ is the resistivity and ϵ is the permittivity of a conductor. For most conductors this border frequency is in the petahertz range [59] e.g. for copper $10^{18}\ Hz$

[59]: Jordan et al. (1968), *Electromagnetic waves and radiating systems*

[60]: Clayton (2006), *Introduction to Electromagnetic Compatibility*

$$\delta = \sqrt{\frac{2\rho}{\omega\mu}} \tag{3.1}$$

The second assumption is that the reflecting surface is a good conductor, which means that the impedance of the reflector is far lower than that of free space η_0 and that the conductivity is far higher than the permittivity [60]. The intrinsic impedance of the reflector and the wave impedance of free space calculates to

$$\hat{\eta} = \sqrt{\frac{j\omega\mu}{\sigma + j\omega\epsilon}} \tag{3.2}$$

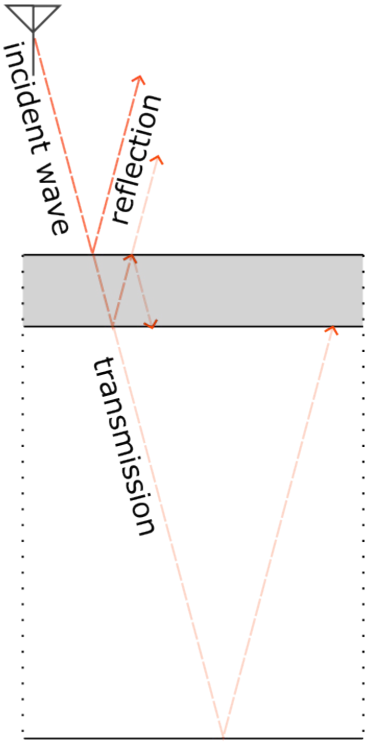

Figure 3.1: Transmitted and reflected waves on the surface and inside a conducting material.

$$\hat{\eta} = \sqrt{\frac{j\omega\mu}{\sigma}}\sqrt{\frac{1}{1+\frac{j\omega\epsilon}{\sigma}}} \tag{3.3}$$

$$\hat{\eta} \cong \sqrt{\frac{j\omega\mu}{\sigma}} \tag{3.4}$$

$$\eta_0 = \sqrt{\frac{\mu_0}{\epsilon_0}} \tag{3.5}$$

For a 60 GHz radar illuminating a piece of 1 mm thick sheet metal, the skin depth calculates to

$$\delta = \sqrt{\frac{2 \cdot 70 \cdot 10^{-8}\Omega m}{10\pi \cdot 10^{-3} \cdot 60 \cdot 10^{9} Hz}} = 0.0273\mu m \tag{3.6}$$

and thus much smaller that the material thickness. The outer medium is air with a wave impedance of air is 376.73 Ω and the electrical impedance of the inner material calculates to 9 Ω for SAE 1045 Steel. This means that both assumptions hold true.

Under those two assumptions, the transmission coefficient between incoming electric field and electrical field propagating through the medium becomes

$$\frac{\hat{E}_1}{\hat{E}_i} \cong \frac{2\hat{\eta}}{\hat{\eta}+\eta_0} \tag{3.7}$$

The coefficient of the wave leaving the material and the wave propagating through the medium is therefore equation 3.8.

$$\frac{\hat{E}_t}{\hat{E}_1} \cong \frac{2\eta_0}{\hat{\eta}+\eta_0} \tag{3.8}$$

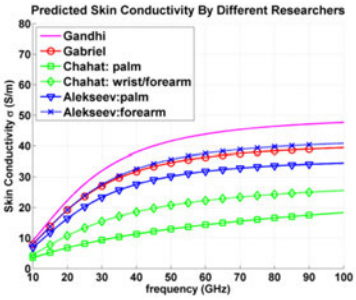

Figure 3.2: Conductivity of human skin based on multiple models dependent on frequency

Because of the assumption that the impedance of free space is much larger than that of a conductor, the transmission into the medium is close to zero. Therefore, nearly all the energy stored in the electric field will be reflected. In contrast, the magnetic field is primarily reflected at the second material border.

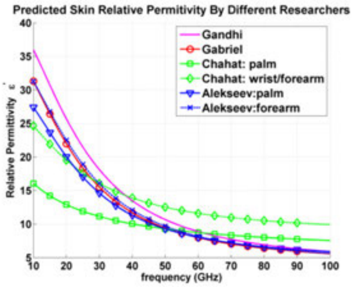

Figure 3.3: Permittivity of human skin based on multiple models dependent on frequency

3.2.2 Reflectivity of Human Tissue

While the reflectivity of a non-homogeneous material like skin can only be approximated, its conductivity and permittivity of human tissue is dependent on multiple measurement parameters. This includes thickness, temperature and the composition of the skin amongst others. It can be said that the relative permittivity of skin decreases with the increase of frequency, whereas the conductivity of the skin increases with higher frequency. Therefore, the reflectivity of skin is also highly dependent on the illuminating frequency. Fig. 3.4 shows the power reflection coefficients at the air and skin interface at 60 GHz for parallel and perpendicular polarized components using various skin model parameters developed by the aforementioned researchers. The results reveal that 34%-42% of the normal incident power is reflected at the skin surface at 60 GHz. The power reflection coefficients vary by 20% when different dielectric model parameters are applied [61].

[61]: Wu et al. (2015), 'Safe for Generations to Come: Considerations of Safety for Millimeter Waves in Wireless Communications'

3.2.3 Differentiation Based on Material Properties

The reflected power needs to be radiated back to the radar receiver. This depends on the kind of surface, as the smoothness impacts the amount of specular and scatter reflection emitting from the reflector. Apart from that, it can be concluded that metal and materials like skin have sufficient difference in their reflected power to differentiate them from each other but, both emit enough reflections to be detected.

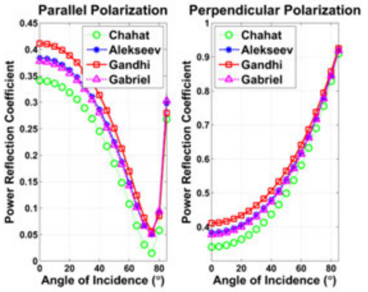

Figure 3.4: Reflected power of human skin dependent on polarization and angle of incidence based on different models

3.3 MIMO-SAR Sampling

Sampling with a MIMO aperture along a track constructs an array consisting of copies of the original physical array. The resolution considerations and the limitations for sampling distance to be able to produce coherent measurements apply to both the antenna array design and the SAR process.

3.3.1 Spatial and Range Resolution

The achievable resolution is, like in camera systems, important for 3D SAR imaging. [62] suggests that the range resolution in Z-axis is primarily defined by the system's bandwidth. It can be expressed as

$$\Delta_z = \frac{c}{2B} \tag{3.9}$$

[62]: Zhuge et al. (2011), 'A Sparse Aperture MIMO-SAR-Based UWB Imaging System for Concealed Weapon Detection'

where B is the frequency bandwidth of the FMCW system. Equation 3.9 shows, that the frequency sweep bandwidth should be fully used. The effect is however limited as it is only indirectly proportional. The same proposition as in [46] is made, stating that

[46]: Sheen et al. (2001), 'Three-dimensional millimeter-wave imaging for concealed weapon detection'

the resolution in x and y direction is defined by:

$$\Delta_{x/y} = \frac{c \cdot R_z}{f_c \cdot L_{x/y}} \tag{3.10}$$

where $L_{x/y}$ defines the length of the effective aperture in x and y direction and R_Z is the range to the target. A SAR system moving on one axis is only expanding its virtual antenna aperture in that direction. The resolution orthogonal to the movement direction is limited to the extent of the physical antenna array. The aperture in the driving direction can be infinite, therefore the approximation below has to be utilized where Δ_x is the cross-range resolution, λ_c is the wavelength at center frequency and Θ_{beam} is the beam width of the antenna.

$$\Delta_x \approx \frac{\lambda_c}{4sin(\Theta_{beam}/2)} \tag{3.11}$$

Alternatively, the beam width geometrically defines a maximum aperture size depending on the distance of the target. If the electromagnetic waves returning from a target are physically not able to reach the antenna, no image can be formed. The maximum size for a parallel target plane is given by the following equation.

$$L_{x_{max}} = 2\frac{tan(\Theta_{beam}/2)}{R_{target}} \tag{3.12}$$

3.3.2 Spatial sampling distance

Image reconstruction and the previous gathering of data require a discretization of analogous data. For this reason, the Nyquist sampling criterion needs to be satisfied. The amount of sampling needed along the aperture is determined by a number of factors such as target range, size of the targets, wavelength and others. The aperture is the track of the robot moving inside its environment. The spatial Nyquist criterion is satisfied if the phase shift from one sample point to the next is less than π rad. This is equivalent to the temporal sampling theorem, where a sampled rotating pointer must be sampled after turning π rad to specify its turning frequency. Increasing the phase shift above that difference would create aliasing. This leads to the following equation, where Δx is the maximum sampling distance and the $2\pi f/c$ is the temporal angular frequency divided by the speed of light [46].

[46]: Sheen et al. (2001), 'Three-dimensional millimeter-wave imaging for concealed weapon detection'

$$2\pi f_c \frac{2 \cdot \Delta x}{c} < \pi \tag{3.13}$$

It is trivial to formulate, that a pointer angle at a time t is described with equation 3.14 and it must not turn more than π rad.

$$\Theta(t) = 2\pi f_c t = 2\pi f_c \frac{1}{f_s} \leq \pi \tag{3.14}$$

The sampling time t is therefore described by $\frac{1}{2f_c}$. The center frequency f_c can be replaced by the sampling distance traversed with the speed of light as in equation 3.15

$$\frac{1}{2f_c} = \frac{\lambda}{2c} \tag{3.15}$$

The factor 2 is introduced in equation 3.13 as the wave travels to the point and back to the aperture. The most restrictive condition for close objects is therefore described as

$$\Delta x < \frac{\lambda}{4} \tag{3.16}$$

for two sampling positions, receiving a signal at 90 degrees, the largest possible incoming angle. Most antennas have lesser beam opening angles and the target is often in front of the aperture, resulting in a more realistic sampling distance of $\lambda/2$. A detailed graphical representation of this effect can be observed in figure 3.5.

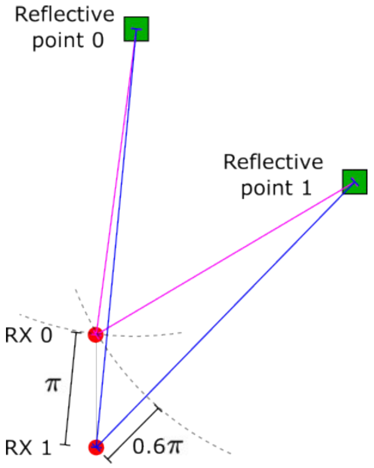

Figure 3.5: Propagation path length differences to antennas for different incident angles

Steinberg [63] also expresses a sampling distance of less than $\lambda/2$ to prevent unwanted grating lobes in the radiation characteristic of the synthetic antenna. They would severely reduce contrast in the picture. Analogues to time signal sampling where the sampling theorem must satisfy two samples per one period of a samples signal, in the spatial realm two frequency samples are per range resolution cell as [46] finds. Consequentially, the number of frequency samples N_f for one per range resolution cell must satisfy the following condition.

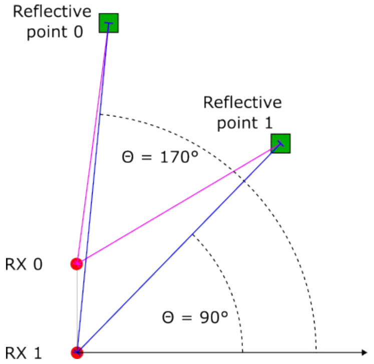

Figure 3.6: Different antenna opening angles influencing the path length differences and therefore the spatial sampling distance

$$N_f > \frac{4R_{max} \cdot B}{c} \tag{3.17}$$

This is congruent with the practical implementation of Texas Instruments radar sensors [64] which translates the sampling theorem to the following equation where f_s is the sampling frequency of the

[63]: Steinberg (1976), 'Principles of aperture and array system design: Including random and adaptive arrays'

[46]: Sheen et al. (2001), 'Three-dimensional millimeter-wave imaging for concealed weapon detection'

[64]: Rao (2017), *Introduction to mmwave Sensing: FMCW Radars*

IF ADC, c is the speed of light and S is the frequency ramp speed of the FMCW frequency sweep in Hz/s.

$$R_{max} = \frac{f_s c}{2S} \tag{3.18}$$

3.4 Technical Aspects of Floor Logistic Robots

The previous section detailed the requirements for sampling distances, achievable resolutions in both range and x-y-direction. These fairly strict demands have to be brought into agreement with specifications of contemporary driver-less cooperative industrial robots. The list of specifications includes the travelling speed as it poses requirements for the sampling distance, the methods of navigation and the accuracy of position detection. The reasons for this are elaborated below.

3.4.1 Measurement Speed

Modern transport systems and co-bots such as [65][66][67] move with a top speed of up to 2 m/s. This means that the robot equipped with a FMCW radar with a center frequency of 62 GHz needs about 1.2 ms to travel the most liberal $\lambda/2$ sampling distance. While the maximum frequency sweep slope of a voltage controlled oscillator ranges from $50-80$ $MHz/\mu s$ and will therefore take $50\mu s$ to cover a bandwidth of 4 GHz, all radar processing and data transmission to the imaging system must not take longer than one millisecond. As detailed in 2.2 this time requirement can substantially be reduced by employing MIMO radars with multiple equispaced RX antennas in the movement direction which simultaneously receive the reflected signal. TI's IWR radar sensors feature up to 4 RX channels which can even be aggregated to a system of 4 sensors, resulting in 16 RX channels per transmitter. This would extend the available time to 19.2 ms while due to parallel ADC sampling, this will still take 50 μs to record the reflected data. The amount of data to be transmitted increases linearly, but tasks such as triggering, connection buildup or file handling will only occur once. The time accounted for post-processing is highly dependent on the required refresh interval for a real time system. It only plays a secondary role if the post-processing is done independent of the robot movement, such as mapping data to insert into an environment model.

[65]: (), *MiR1350 - The most powerful AMR from MiR to date*

[66]: Nipper (), *The compact automated guided vehicle system for pallet transport*

[67]: Robotics (), *Induros - Your superior AMR solution for intralogistics and logistics*

3.4.2 Movement Path

The algorithm complexity depends on the robot's way of finding a path between two points. Continuous rotation while moving or omnidirectional movement induce complex interpolation efforts and will form non-planar apertures. These complexities can be significantly reduced by constraining the robot to movements in a ninety degree angle to the radar aperture. A new image is started after each rotation onto a new straight path to another point in the room. Imaging and transforming the resulting image can be done with well known coordinate transformations.

3.4.3 Motion Detection

As shown in 3.3.2, focusing a SAR image in 3-D space, especially in the close range domain, requires the knowledge of the exact position of each sampling point. A robot carrying a radar system therefore needs to accurately track its position along with speed and rotation. This can be implemented by sensor fusion with inertial motion sensor, external surveillance and accurate movement on a calculated path. The radar itself can not be used for this task as Range-Doppler radars to measure distance and velocity are subject to the aforementioned range resolution limitations as detailed in 3.3.1 and offer velocity resolutions in the domain of meters to decimeters [68] depending on the observation time.

[68]: Lee et al. (2010), 'A Fully-Integrated 77-GHz FMCW Radar Transceiver in 65-nm CMOS Technology'

3.5 Formulated Research Question

The demand for enhanced perception domains for robot-human cooperation and coexistence as well as a possible target robotic system is detailed in chapter 1. Literature and current research concerning possible approaches to this problem are reviewed in chapter 2 with focusing especially on radar, as several enhancements have been made. Those are miniaturization and integration of hardware components, availability of millimeter wave technologies and the resulting resolution improvements for close range usage. Chapter 2.3 further focused on imaging radars and algorithms, as they are a much smaller field in close range applications than the classic FMCW approach detailed in section 2.1. This chapter features a general assessment of usefulness of radar sensors for the aforementioned application. It also points out that radar in the millimeter band has a limited resolution for shape detection compared to cameras and details the feasibility of reflectivity differentiation between different materials, especially human skin and conducting materials. It may therefore be used to support cameras or other sensors in gaining knowledge, especially in realms which they cannot physically observe. That is, for example objects being shaded by materials not transparent in the visual spectrum or not clearly identifiable by their visual representation. The last section of this chapter, lays out the limitations and challenges for imaging radars analyzed by previous research. Based on those previous chapters the opportunity for further research presents itself. A combination of technologies from high resolution imaging approaches such as body scanners and satellite imagery with close range, low latency industrial applications offer a less studied field in general.

The methods in chapter 4 will explore the selection of a close range imaging algorithm in combination with recently developed low cost radar systems. Limitations in the sampling speed domain are explored as they impact the applicability on a robotic system. The speed and mathematical complexity need to be taken into account as they heavily impact the frame rate. Evaluation needs to be both possible with viewing hidden objects and differentiating between dielectrics and metals. As shown in section 3.2 the relevant subjects reflect enough radiated power to be both imaged and differentiated. The low resolution cause by a fixed physical aperture size in one direction, needs to be considered. The resulting challenges for a successful implementation, while not being solved in this work, should be clearly identified and presented as a conclusion for further evaluation.

If the researched approach turns out to be feasible. it can result in a cost-effective and novel perception enhancement, which gains relevance in an emerging robot presence in industrial environments and more applications in general.

Methods 4

This chapter formulates methods that make a scientific evaluation of the research question possible. The limitations specified in the previous chapter are taken into account and refined by this work.

4.1 Hardware Selection

With the consideration of an economically viable solution, a fully integrated radar sensor is chosen which offers a wide bandwidth to maximize the range resolution of the system. As the robot only moves the system in one direction, a MIMO system with a maximum number of antennas in the direction orthogonal to the floor and a distance between the antennas of no more than the spatial sampling distance in chapter 3.3.2 is chosen. The sampling distance limit is not clearly defined, as it depends on the opening angle of the antennas in use and the region of interest. That is why at least two different physical antenna distances in the vertical direction have to be evaluated. The sampling distance in movement direction in contrary can be freely chosen if the physical aperture has no extent in movement direction. On the other hand, employing a MIMO array with an extent parallel to the movement direction can drastically reduce the overall sampling interval, but also defines the sampling distance to the half of the physical antenna distance as is hereinafter explained. For this reason, at least two antenna configurations in movement directions are evaluated against each other. Two layout are chosen, one being a line of antennas, the other forming a rectangular aperture to explore both effects.

An off the shelf radar sensor is chosen, as the price point is one of the most important secondary arguments for industry applicability. It has a specified frequency band for wideband operation. Most common bands in the millimeter wave region are 24 GHz, 60 GHz as well as 77 GHz. While the 24 GHz centered ultra-wideband is nowadays prohibited to new products by the European Telecommunication Standards Institute and Federal Communications Commission, the 77 GHz band is used for automotive applications. Strong regulations apply to industrial or other commercial usages to reduce interference with traffic safety. Consequentially, the only remaining option for an industrial open space sensing solution is the 60-64 GHz band [69]. No commercially available, certified radar ICs exist, because higher frequency bands are currently under regulatory development.

[69]: Jacobi et al. (2018), 'Choosing 60-GHz mmWave sensors over 24-GHz to enable smarter industrial applications'

It is detailed in 2.1 that the state-of-the-art radar sensors offer the possibility to configure the steepness of the frequency sweep and its duration. Additionally, multiple repetitions of that sweep (in one frame) for one sampling point as well as multiple frames are configurable to gain azimuth and velocity information. A velocity Fourier transformation is not to be researched for an imaging approach and the azimuth and elevation information will be covered by spatial imaging, therefore the amount of chirps and frames is reduced to the minimum to generate the minimal amount of data and speed up sampling time. The number of samples is narrowly defined by the Nyquist criterion, as stated before. Combining both the resolution limitations of a fast chirp radar and the minimum number of samples required presents a problem:

To achieve maximum range resolution, the sensors full bandwidth B is exploited. This bandwidth is swept with a frequency slope S. Combining these two limitations (see chapter 3.3.2) results in

$$N_f > \frac{2f_s \cdot B}{S} \tag{4.1}$$

The limiting factor of the hardware is the theoretically required sampling frequency of the ADC. That means that in one frequency ramp, the ADC also needs to sample the required samples in 4.1 with the sampling rate f_s

$$t_{adc} = \frac{N_f}{f_s} \tag{4.2}$$

While also

$$B = S \cdot t_{slope} \tag{4.3}$$

The ADC sampling time has to be shorter than the slope time, as the sampling would otherwise interfere with the next sweep.

$$t_{slope} > t_{adc} \tag{4.4}$$

But if the number of samples N_f in equation 4.1 is replaced by the limit formulated above and t_{slope} by B/S, it can be seen that either the Nyquist criterion or the technical limitations can be satisfied. They can not be fulfilled simultaneously, as inserting the equation results in

$$\frac{B}{S} > \frac{2f_s \cdot B}{f_s \cdot S} = \frac{2B}{S} \tag{4.5}$$

which can never hold true. Therefore, especially sampling points on the edges of the aperture will necessarily form unwanted ghosts. The visual limitations of these violations are empirically shown.

From chapter 3 it is also known, that the encountered objects can be distinguished by their reflectivity. The algorithm chosen must be able to calculate that information. The chosen method for sampling back-projected waves from the surroundings will be transformed into a calculation of the reflectivity itself.

4.2 Algorithmic Basis

The follow section details the algorithmic groundwork for MIMO-SAR applications for both monostatic and multi-static antennas systems as well as monochromatic and broadband signal operations.

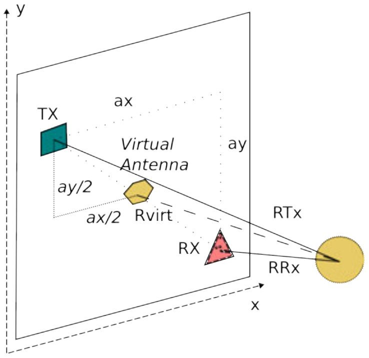

Figure 4.1: Location of a monostatic virtual antenna derived from a bistatic RX and TX setup

4.2.1 The Virtual Monostatic Aperture

When using a MIMO array for SAR purposes, additional complexity arises from having transmitter and receiver pairs at differing locations. Those pairs are combinations of i transmitters $(0, \ldots, I)$ and j receivers $(0, \ldots, J)$ each having spatial coordinates $TX_i = (x_i|y_i|z_i)$ and $RX_j(x_j|y_j|z_j)$. An electromagnetic wave travelling from TX_i to a target point $P(x|y|z)$ to RX_j so the distance $R_{TX_iP} = |P - TX_i|$ and $R_{PRX_j} = |RX_j - P|$ will travel $R_P = R_{TX_iP} + R_{PRX_j}$. A simplification for this problem is to create a virtual bistatic element at the midpoint of RX_j and TX_i by assuming that the target distance is large compared to the distance between the phase centers of transmit and receive. The construction of such virtual antenna A_{ij} at $\frac{1}{2}(RX_j + TX_i)$ with a range $R = 2|P - A_{ij}|$to the target is valid if difference between exact range and approximated range is only a small fraction α of the wavelength ($|TX_i - RX_j| \leq 2\sqrt{\alpha\lambda R}$) [70].

[70]: Ender et al. (2009), 'System architectures and algorithms for radar imaging by MIMO-SAR'

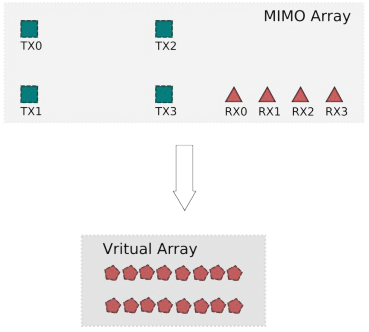

Figure 4.2: Transformation of an exemplary MIMO array with four RX and 4 TX channels and a resulting 16 virtual monostatic channels.

Therefore, a MIMO array consisting of I receivers and J transmitters can be simplified into a virtual array of $I \cdot J$ virtual monostatic antennas

The wave then originates from the virtual phase center, and the round trip distance is calculated from this point to the scatterer at the target. This simplification is useful to form a uniform array for the calculation of the following algorithm. The accuracy of the round-trip distance can be improved by adhering to the virtual phase centers but calculating the round trip distances from the actual receiver and transmitter locations [71].

[71]: Yanik (2020), 'Development and Demonstration of MIMO-SAR mmWave Imaging Testbeds'

4.2.2 Sampling with a Monostatic Monochromatic Aperture

The simplification, which is elaborated in the previous section, can be used to deduce the following. Assuming that there is a single transceiver emitting a signal with a fixed frequency at the position $(\hat{x}, \hat{y}, \hat{z})$, a reflective target parallel to the aperture at position $(x, y, 0)$ will back-scatter at that frequency. This is true if the target is not moving and thereby inducing a Doppler-shift in the frequency. The synthetic aperture which emits the signal has a constant distance in z-direction to the target. The distance from the transceiver to a point on the target is then $d(x, y)$.

$$d(x, y) = \sqrt{(\hat{x} - x)^2 + (\hat{y} - y)^2 + \hat{z}^2} \tag{4.6}$$

A wave reaching the target at the speed of light c at point (x, y) will be attenuated by the reflectivity function of the target at a point on the target $r(x, y)$. All reflected waves reaching the transceiver from all the coordinates on the target plane will have traveled two times the trip distance at the speed of light. Omitting the amplitude decay, they can be described by a superposition at the transceiver location

$$s(\hat{x}, \hat{y}) = \iint r(x, y) e^{2\pi f \cdot \frac{2d(x,y)}{c}} dx dy \tag{4.7}$$

Considering the term

$$e^{2\pi f \cdot \frac{2d(x,y)}{c}} \tag{4.8}$$

to be a wave radiating from a point source at $(\hat{x}, \hat{y})$ it can be decomposed in its plane wave components. This is only valid if the target is far enough so that the wavefront reaching the target can be approximated to be a planar wave.

$$e^{-jk2d(x,y)} = \iint e^{j[k_{\hat{x}}(\hat{x}-x)+k_{\hat{y}}(\hat{y}-y)+k_{\hat{z}}\hat{z}]} dk_{\hat{x}} dk_{\hat{y}} \tag{4.9}$$

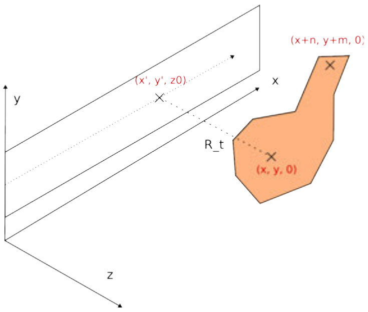

Figure 4.3: Monochromatic scanning of a target parallel to the x/y-plane of the SAR aperture

$k_{\hat{x}}$ and $k_{\hat{y}}$ represent the Fourier-transform variables for both $\hat{x}$ and $\hat{y}$. The term 4.9 when inserted in 4.7 results in the following.

$$s(\hat{x},\hat{y}) = \iint r(x,y) \iint e^{j[k_{\hat{x}}(\hat{x}-x)+k_{\hat{y}}(\hat{y}-y)+k_{\hat{z}}\hat{z}]} dk_{\hat{x}} dk_{\hat{y}} dx dy \tag{4.10}$$

As the following two rules hold, the integrals can be interchanged and rearranged into 4.13. By this rearrangement, it gets obvious, that the bracketed term represents the Fourier transformation of the two dimensional reflectivity function.

$$\int f(x)\left[\int g(x,y)dy\right]dx = \int \left[g(x,y) \cdot f(x)dx\right]dy \tag{4.11}$$

$$\int f(x)g(y)dx = g(y)\int f(x)dx \tag{4.12}$$

$$s(\hat{x},\hat{y}) = \iint \underbrace{\left[\iint r(x,y)e^{-jk_{\hat{x}}x}e^{-jk_{\hat{y}}y}dxdy\right]}_{R(k_{\hat{x}},k_{\hat{y}})} e^{j(k_{\hat{x}}\hat{x}+k_{\hat{y}}\hat{y}+k_{\hat{z}}\hat{z})}dk_{\hat{x}}dk_{\hat{y}} \tag{4.13}$$

With the resulting term 4.13 and another rearrangement for recognisability, the function simplifies to

$$s(\hat{x},\hat{y}) = \iint R(k_{\hat{x}},k_{\hat{y}})e^{j(k_{\hat{x}}\hat{x}+k_{\hat{y}}\hat{y})}e^{jk_{\hat{z}}\hat{z}}dk_{\hat{x}}dk_{\hat{y}} \tag{4.14}$$

The inverse two dimensional Fourier transform of a function F and its inverse is defined by

$$\iint F(k_x,k_y)e^{jk_x x}e^{jk_y y} = \mathscr{F}_2^{-1}(F(k_x,k_y)) \tag{4.15}$$

$$\mathscr{F}_2^{-1}\left\{\mathscr{F}_2\{f(x,y)\}\right\} = f(x,y) \tag{4.16}$$

By applying a Fourier transformation to both sides of 4.14 and shifting the remaining exponential function to the recorded signal, the reflectivity function can be retrieved by calculating the inverse Fourier transformation on both sides, resulting in

$$r(x,y) = \mathscr{F}_2^{-1}\left\{\mathscr{F}_2\{s(\hat{x},\hat{y})\}e^{-jk_z\hat{z}}\right\} \tag{4.17}$$

The $s(x,y)$ function is directly the recorded signal of a monostatic transceiver. The distance of the transceiver to a parallel planes is assumed to be constant. The only remaining part is the variable k_z. From the previous decomposition of a plane wave into its three axial components, it is known that

$$(2k)^2 = (2\frac{2\pi f}{c})^2 = k_x^2 + k_y^2 + k_z^2 \tag{4.18}$$

resulting in k_z being

$$k_z = \sqrt{4k^2 + k_x^2 + k_y^2} \tag{4.19}$$

k_x and k_y are now the spatial sampling frequencies in the target domain.

4.2.3 Sampling with a Monostatic Wide-band Aperture

Instead of using only a monochromatic radar system a FMCW radar is selected. It sweeps over a defined, broad bandwidth. This approach can be extended to fully calculate not only the reflectivity function of a 2D plane but of 3D space.

Under the assumption of a mono-static transceiver at $(\hat{x}, \hat{y}, \hat{z})$ moving on a planar aperture in front of free space defined by coordinates (x, y, z), the round-trip distance $d(x, y, z)$ to any point in this space is calculated with the three-dimensional theorem of Pythagoras as

$$d(x, y, z) = 2 \cdot \sqrt{(\hat{x} - x)^2 + (\hat{x} - y)^2 + (\hat{z} - z)^2} \tag{4.20}$$

As the wave is travelling with the speed of light, the round-trip delay is $t(x, y, z) = d(x, y, z)/c$. The response measured by the transceiver is therefore a three-dimensional integral over all points subtended to the aperture. Each point in space modulates the transmitted signal by its reflectivity function $r(x, y, z)$, the amplitude decay A and delays it by its round-trip delay $t(x, y, z)$. Compared to the previous section, the reflected signal is also extended to all frequencies in the chirp. The amplitude decay has little impact on the imaging abilities of the function and is therefore set to 1. The response reads

$$s(f, \hat{x}, \hat{y}) = \iiint r(x, y, z)e^{-j2\pi f t(x,y,z)}dxdydz \tag{4.21}$$

The exponential term is equal to a spherical wave with a frequency f and an amplitude defined by the time travelled from the point of emission. A fixed transceiver is selected at position $(\hat{x}, \hat{y}, \hat{z})$. This transceiver will receive a reflected plane wave from a point (x, y, z), which has traveled the length of the vector to the transceiver. A planar wave or its travelling orthogonal vector can be decomposed in its three components, resulting in a superposed planar wave [72].

[72]: (2013), *3D Wave Equation and Plane Waves / 3D Differential Operators*

$$q(\hat{x}, \hat{y}, \hat{z}) = e^{-jk_{\hat{x}}\hat{x} - jk_{\hat{y}}\hat{y} - jk_{\hat{z}}\hat{z}} \tag{4.22}$$

As the aperture is fixed in the z-layer, integrating over both the x and y wavenumber components results in

$$e^{-jk\sqrt{\hat{x}^2+\hat{y}^2+\hat{z}^2}} = \iint q(\hat{x}, \hat{y}, \hat{z})\bigg|_{\hat{z}=const} dk_{\hat{y}} dk_{\hat{x}} \tag{4.23}$$

Injecting the target point in space into the x,y and z components and inserting a factor two as the round-trip distance is taken, the decomposition of function 4.23 into plane wave components can be undertaken. Round-trip factor can later be taken care of when using the dispersion relation of plane waves. With the same rearrangement as in 4.13, the integrals are swapped. Now the three-dimensional integral represents the reflectivity function's spatial Fourier transform

$$s(f, \hat{x}, \hat{y}) = \iint \underbrace{\left[\iiint r(x, y, z) e^{-j(k_{\hat{x}}x + k_{\hat{y}}y + k_z z} dx dy dz \right]}_{R(k_{\hat{x}}, k_{\hat{y}}, k_z)} e^{-jk_{\hat{x}}x + k_{\hat{y}}y + k_z\hat{z}} dk_{\hat{x}} dk_{\hat{y}} \tag{4.24}$$

The inverse two-dimensional Fourier transform $\mathscr{F}_2^{-1}$ is defined in the following way

$$f(x, y) = (2\pi)^{-1} \iint F(k_x, k_y) e^{jk_x} e^{jk_y} dk_x dk_y \tag{4.25}$$

Formula 4.24 now represents the two dimensional inverse Fourier transform of the three dimensional Fourier transform of the reflectivity function

$$\iint R(k_{\hat{x}}, k_{\hat{y}}, k_z) e^{-jk_{\hat{x}}x} e^{jk_{\hat{y}}y} e^{k_z\hat{z}} dk_{\hat{x}} dk_{\hat{y}} = \mathscr{F}_2^{-1}\left\{ R(k_{\hat{x}}, k_{\hat{y}}, k_z) e^{jk_z\hat{z}} \right\} \tag{4.26}$$

Finally the original function $s(f, \hat{x}, \hat{y})$ equals the inverse Fourier transform of the reflectivity function. Transforming both sides again gives

$$\mathscr{F}_2\left\{ s(f, \hat{x}, \hat{y}) \right\} = R(k_{\hat{x}}, k_{\hat{y}}, k_z) e^{jk_z\hat{z}} \tag{4.27}$$

While the spatial Fourier transform factors of x and y are known,

k_z is not. Applying the three dimensional theorem of Pythagoras again, f can be represented as a function of k_z. Notice the $2k$ for the round-trip distance

$$2k = 2\frac{2\pi f}{c} = \sqrt{k_x^2 + k_y^2 + k_z^2} \tag{4.28}$$

$$k_z = \sqrt{(\frac{2\pi f}{c})^2 - k_x^2 - k_y^2} \tag{4.29}$$

Therefore

$$\mathscr{F}_2\left\{s(f, \hat{x}, \hat{y})\right\} = R(k_{\hat{x}}, k_{\hat{y}}, k_z)e^{\sqrt{(\frac{2\pi f}{c})^2 - k_x^2 - k_y^2}} \tag{4.30}$$

The inverse, three dimensional Fourier transform of the equation above then yields the reflectivity function in the three dimensional coordinate system

$$r(x, y, z) = \mathscr{F}_3^{-1}\left\{\mathscr{F}_2\left\{s(f, \hat{x}, \hat{y})\right\}e^{-\sqrt{(\frac{2\pi f}{c})^2 - k_x^2 - k_y^2}}\right\} \tag{4.31}$$

4.3 Mathematical Limitations

Up until now, this algorithm is designed for continuous data, which is not applicable to the problem at hand. The equispaced sampling in x and y allows for a relatively easy conversion into the discrete domain. The z axis can not be equispaced as waves propagate on a spherical path. Thus, for linear movement in x and y direction and equispaced sampling points, all samples need to be interpolated in the z domain. This poses two serious limitations, which are not handled in this work. While a robot may be forced to travel only on straight lines, it may hamper it's pathfinding capabilities. A planar aperture is thus a coarse approximation and would in reality be a three-dimensional aperture with a very narrow extent in y direction. Further research is needed to be able to create coherent pictures with the antenna also moving in z direction.

The model robot also does not rotate. A turn of the robot would induce another variable, which is the intermediate rotation of the whole coordinate system between two sampling points. These two issues are also visualized in figure 4.4. Solving those limitations does not only require further mathematical development of the algorithm, but also very precise processing of the robot's current

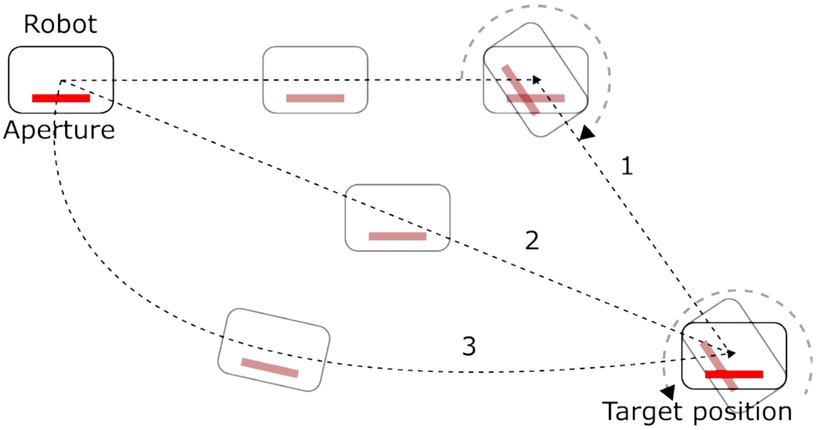

Figure 4.4: Visualization of different movement possibilities of robots. 1) is a robot moving on a straight path, rotating for every direction change. The antenna aperture is always parallel to the movement direction. 2) is an omnidirectional robot forming a three-dimensional synthetic aperture. 3) is a robot rotating while adhering to a arbitrary path.

position. Data of an accurate IMU as well as a range radar should be merged to accurately define a position by a tenth of a millimeter.

4.4 Summary

The previous paragraph reviews the algorithmic basis for a conversion of multi static arrays into monostatic virtual apertures, which is limited by the distance of RX elements and TX elements. The recorded data is ready to be processed by the evaluated close range capable image reconstruction algorithm which results in the measured reflectivity of every reflective, non-shaded point [1] in range of a planar synthetic aperture for both monochromatic and wideband operation. The practical implication of the required sampling distance and therefore the requirements for measurement time and processing power need to be evaluated with empirical research. Therefore, two different sets of antennas are chosen in the same frequency band. Both antenna arrays are calibrated using a state-of-the-art calibration method [73][74].

1: Shaded by materials which are opaque in the millimeter wave band

[73]: Ng et al. (2009), ‘A Practical Simple Geometry and Gain/Phase Calibration Technique for Antenna Array Processing’

[74]: Schmid et al. (2013), ‘An FMCW MIMO radar calibration and mutual coupling compensation approach’

Implementation 5

The following section details both the hardware and software components used to implement the proposed methods. It describes the selected parameters which are influenced by the limitations described in 3.3.2 and 3.3.1 as well as those posed by the used hardware. Additionally, the employed open source code and previous works by the Fraunhofer IZM are pointed out below.

5.1 Hardware Components

In this thesis, two different radar interfaces are used. Both are based on the Texas Instruments IWR6843 FMCW transceiver IC. It features three transmitter and four receiver ports. The available bandwidth is 4 GHz, starting from 60 GHz at a total transmitting power of 12 dBm with a maximum frequency slope of 250 $MHz/\mu s$.

The chip combines an ARM-R4F MCU, a C674x DSP and sections for hardware accelerated FFTs, filtering and CFAR processing. While a lot of signal processing can be done on the chip, it is also possible to acquire the raw ADC IF data over an LVDS-interface. Processing large amounts of data in real-time requires an appropriate data sink, which is realized by a Lattice FPGA on the TI DCA 1000 capture board.

5.1.1 DCA1000 Raw Data Capture Board

Capturing raw data directly from the IWR6843 ADC bank with the PC is not possible. The DCA1000 Evaluation module allows capturing all four ADC buffers by transmitting them with either a two or four-lane LVDS signal. The data can then be transferred to the PC via 1-GBps Ethernet and the MMWAVE-STUDIO software suite, or directly to a SD-Card. In the other direction, the DCA1000 board also functions as a configuration interface with a wide range of settings, such as chirp configuration, sampling rate, calibration and interrupts. It features two USB FTDI ICs which emulate 5 COM ports for communicating with the radar board attached with a 60 pin high density connector and two UART ports related to the

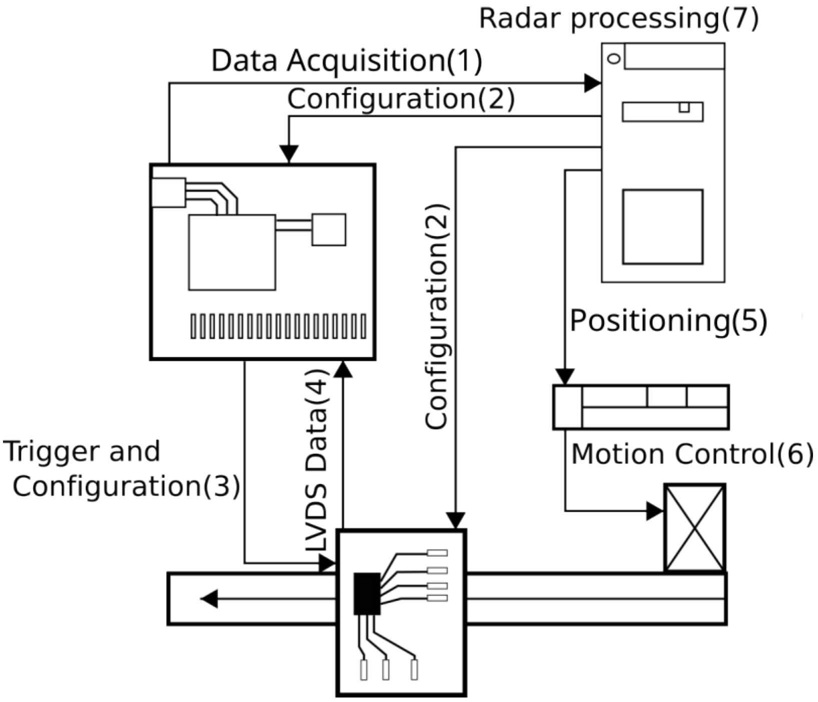

Figure 5.1: The data acquisition over interface is launched over Ethernet (1). The PC configures the DCA1000EVM board and the radar board(2). Further configuration data and the trigger signal is sent to the radar board (3). The captures data is transferred to the DCA1000EVM over the 2-line LVDS interface (4). The PC sends new positioning data to the controller (5) which starts the motor (6). The radar data is afterward processed on the PC(7).

FPGA itself. Further configuration for the board itself is done with a variety of DIP-switches.

5.1.2 IWR6843ISK Evaluation Board

The IWR6843ISK evaluation board is developed around the IWR6843 chip. It uses four uniformly spaced receiver antennas along the Y-axis. They are each $\lambda/2$ apart from each other. The transmitter elements are placed λ apart from each other, while the middle one is also shifted by λ along the X-axis. The expected elevation resolution is rather small compared to a relatively fine azimuth resolution.

Figure 5.2: The DCA1000 evaluation module featuring a Lattice FPGA and GBit network interface for capturing ADC data directly over LVDS.

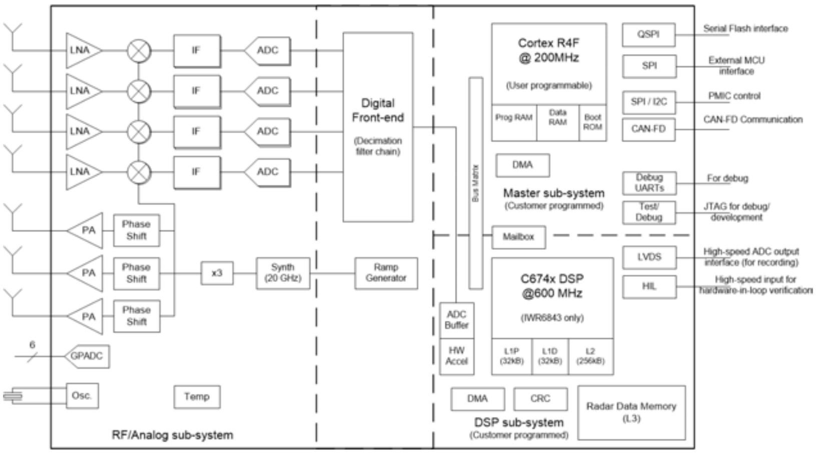

Figure 5.3: Schematic of the IWR6843 radar sensor. The DSP and MCU are located in the programmable DSP sub-system and Master sub-system. Both can read from the ADC buffer, which stores data from the digital front end.

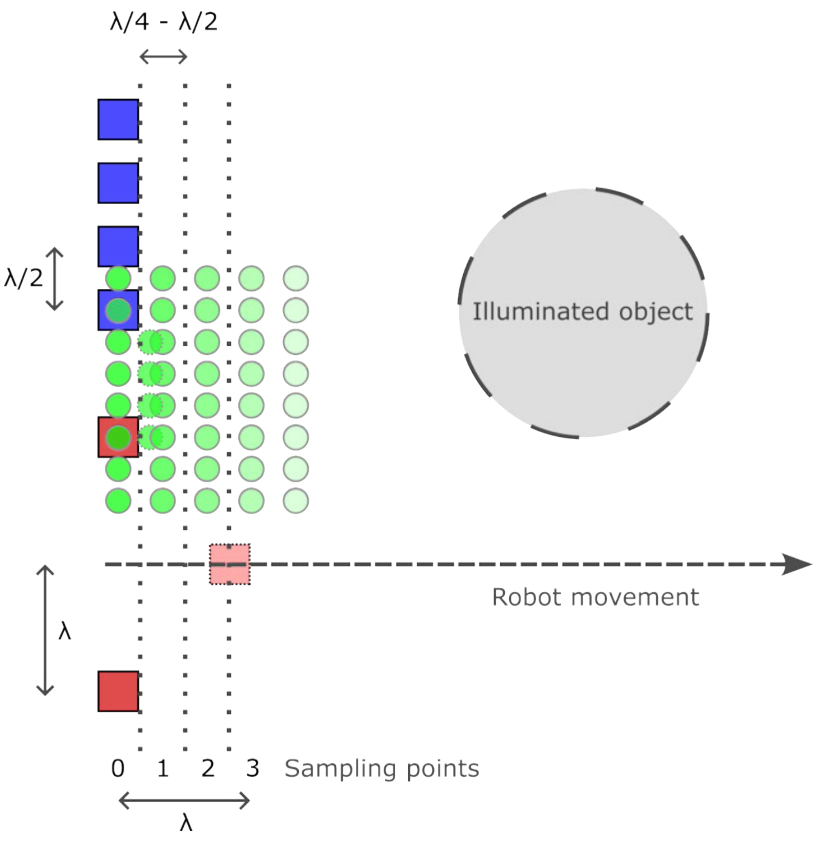

Figure 5.4: IWR6843ISK antennas configuration. The RX antennas are marked in blue, whereas the TX antennas are marked in red. Only the first and third TX antennas are used. The resulting virtual antenna array is marked in green. It will either form a equispaced array or a uniform array, depending on the selected sampling distance. $\lambda/4$ forms a uniform array.

Figure 5.5: The IWR6843ISK module featuring three transmit and four receive antennas connected to a IWR6843 radar sensor.

5.1.3 Custom Evaluation Board

The custom radar module is originally developed for another project at Fraunhofer Institute and uses a different antenna design than the IWR6843ISK while using the same IC. Up until this work, only the correct electronic functioning was tested. It features a row of 3 transmit antennas and a row of four receive antennas which are placed orthogonal to each other. Each antenna is placed in λ distance both in x and y direction. To connect the custom radar interface to both a UART interface and the DCA1000's LVDS port, an additional system board was developed. The DCA1000 connectivity is ensured by using the same connector and board shape like the IWR6843ISK.

5.1.4 Custom Board Connectivity Module

The in-house radar module is developed with all relevant ports externally accessible via plated half-holes. This simplifies the integration into larger system boards or adaptations to various evaluation modules, such as the Raspberry Pi or the Arduino environment. For this reason, the bottom side is completely free of any components and is thus not able to hold the 60 pin high

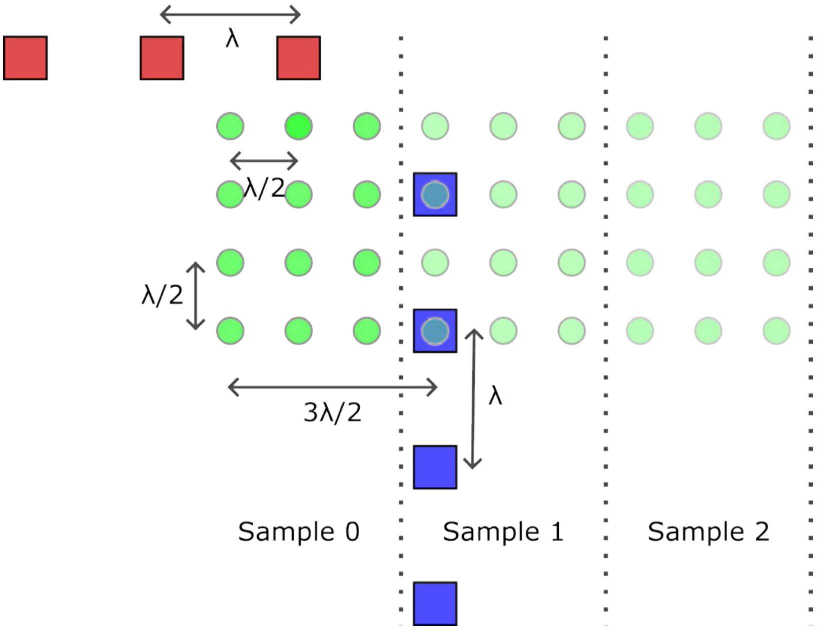

Figure 5.7: Custom board antenna configuration. The RX antennas are marked in blue, whereas the TX antennas are marked in red. Every antenna is used, resulting in 12 virtual phase centers. The resulting virtual antenna array is marked in green. A uniform virtual array is formed, if the sampling distance is $\lambda/2$. The distance between the antenna is larger compared to the IWR6843ISK board, resulting in a more sparse virtual array marked in green.

density connector. Therefore, an adapter board is designed which, apart from connecting the half-holes to the high density bridge, features the following components:

Figure 5.6: The custom radar module with the IWR6843 radar sensor. The orthogonal antenna rows are visible. The module is mounted on an adapter board for the DCA1000 evaluation module. It also features three TX antennas in the vertical direction and four RX antennas in the horizontal direction

Power Supply

The DCA1000EVM board can not supply the IWR6843 radar sensor with adequate power. The adapter board itself features a 3.3 V linear converter and stabilization for the external 5 V power supply. A LED indicator is added to visually validate the external power supply as well as the reduced 3.3 V line to be functional.

Sense on Power Switches

The IWR6843 radar sensor has three so called "sense-on-power" inputs which are used to configure the mode of operation. They have to be set to either functional mode, flashing mode or development mode. The latter is used in combination with the DCA1000EVM. To make the board usable for USB operation, it is mandatory to be able to switch between configurations. For that reason, a DIP-switch bank is implemented and connected to the IWR6843s SOP ports.

UART Operation

To enable both UART connection over the 60 Pin high density bridge and external UART connections, a ribbon cable port was

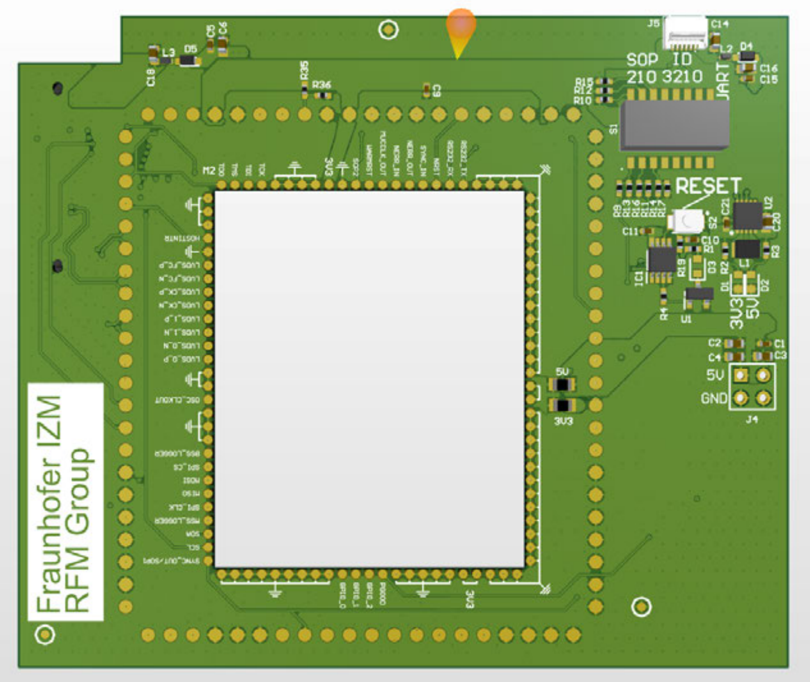

Figure 5.8: The 3D view of the connectivity module designed in AltiumDesigner. The cutout and solder bridges for the custom board and future designs can be clearly seen.

attached to the top side of the board which can be connected to a USB-to-UART adapter to directly connect the adapter board to the PC.

Reset Functionality

The DCA1000EVM board is able to reset the IWR6843 remotely. This only works when the IWR6843 is in development mode. To change the aforementioned SOP indicated modes also require the radar sensor to be power cycled and to be reset. This is why a physical reset button is also placed on top of the adapter board. A LED is added for visual indication.

5.1.5 Linear Rail Motor

The movement of the radar is simulated by fixing the DCA1000EVM and the IWR6843 Boards to a sleigh on a linear rail. A custom adapter was 3D printed for that purpose. The sleigh is moved by tooth belt powered by a stepper motor. With an accuracy of 0.01 mm it can reliably move quarter wavelengths in the V-band which is sufficient for the most restrictive sampling distances evaluated in chapter 3. The rail has a drive range of 1000 mm and thus deemed sufficient to simulate the passing by several targets. Another option of using a solution based on the "High-Z" portal milling machine was implemented by sending GCode over Ethernet but was consequentially put aside although being able to travel a plane of 1000 mm x 500 mm. The machine's weight, slow speed and fixed location did not fit the research questions in this work, but may be of future use for calibrating and testing radars moving on non-linear paths.

The Model is an IAI Corp. RCP2-BA6-I-42P-54-1000-P3-S Motor and rail combination. It is controlled by an IAI Corp. PCON-CA-42PWAI-PN-2-0 control unit and powered by a 24V 5A S-120-24 power supply.

The software shipped with the control unit is sufficient to continuously move the motor to fixed positions with the press of buttons. A fully automated measurement requires an individual solution. The communication between control unit and PC can be implemented with several industrial protocols, the simplest way is to use the ModBus functionality with a serial to ModBus adapter. The control registers can be directly written via ASCII symbols over a standard UART port without any flow control.

An exemplary command is seen below. The meaning of the individual command sections can be followed in table 5.1.

```
:0110990000070E000001900000000100002710006414
```

Table 5.1: Serial command structure.

String	Value	Register	Function
:	-	-	Command prefix
01	1	Axis	0th axis
03	3	Command	Move to a position
9900	-	Start address	First register address to write to
0007	7	Number of registers	Number of consecutive registers
0E	14	Number of bytes	Number of bytes written to consecutive registers
00000190	400	Position	Target position in 0.01 mm
00000001	1	Positioning band	Accuracy of movement in 0.01 mm
00002710	10000	Speed	Sleigh travelling speed in 0.01 mm/s
0064	100	Acceleration	Sleigh acceleration and deceleration in 0.01 G
14	20	CRC Check	Checksum calculated by adding all commands in 2 byte blocks and forming the two's complement

The translation into the aforementioned structure, the calculation of the checksum and UART connection are directly integrated into a Matlab object. This motion controller object is then directly used by the measurement process. The current position of the sleigh can be read from the motor's position register. The implemented library is thus able to move the motor to fixed positions in its position register, move arbitrary distances, and move until the position register of the motor reaches the wanted position. Functionality is implemented to clear the motor's alarm registers. The alarm flags get set if a homing process in interrupted or too much strain is put on the sleigh.

5.1.6 Targets and Calibration Devices

A corner reflector is used to calibrate the radar. It is a geometric form made of three mutually perpendicular, intersecting flat surfaces. Those surfaces are highly reflective for the respective signal and due to the geometry, a wave will always be reflected twice, resulting in a parallel but inverted direction vector compared to the impact vector. There are two edge cases of a ray hitting the reflector. One is a ray reflecting of the outermost area of the surface, which will travel inside the corner reflector long enough such that the propagation time is equal to the second case. That is a wave being reflected at the center (see fig. 5.9). Other targets include metal objects of various surface condition, such as polished and rough. Flange bushings with a wall thickness of λ are placed behind a non-metallic cover. Several other non-conductive objects as well as a human arm are used to evaluate their reflectivity.

The objects which have a size of around 50 mm x 50 mm are varied in height in close range to the radar system to evaluate the resolution in z-direction. They are also varied in their distance in x-direction to make conclusions about the resolution in x-direction. Their y variation is small due to the expected low resolution in y-direction. Additionally, further targets are chosen by either being transmissible to radar waves to simulate hidden objects or metal furniture or devices.

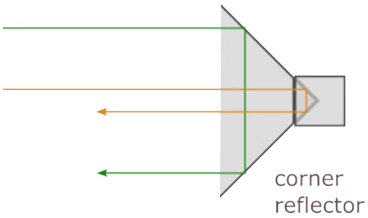

Figure 5.9: Two dimensional corner reflector with two rays being reflected back to the sender while having an equally long propagation path inside the reflector

5.2 Software Components

Apart from the hardware components of the setup, multiple programs are utilized in the measurement setup. Several open source resources are put together by extending them with modules or developing standalone modules communicating with respective application programming interfaces. The different purposes of software modules and their origins are hereinafter listed.

5.2.1 MMWave Studio

MMWAVE-STUDIO is a collection of tools that enhance the evaluation of TI MMWave sensors. MMWave studio is developed directly by Texas Instruments. These tools are capable of configuring hardware connections and data acquisition and designing and prototyping chirps for FMCW radar sensor. It provides the ability to configure and control MMWave sensor modules and collect analog-to-digital data for analysis. It also offers the possibility of doing basic post-processing and visualization of ADC data. A Windows API in .dll form is provided as well as a command line interface which in this work is used for external control by the measurement software. The main Matlab measurement software is connected to the MMWave studio application and can send a variety of Lua commands to the DCA1000EVM and IWR6843ISK board. Those include configuration of the radar sensor, LVDS data format definition and chirp parameters. Lua commands are also used to trigger the board and start the ADC recording when the board reaches a sampling position.

5.2.2 Matlab Imaging Toolbox

The MIMO-SAR-MMWave-Imaging-Toolbox (SAR-Toolbox) is a tool provided by the researcher Muhammet Emin Yanik for a 79 GHz radar sensor. The three main components are the multistatic to monostatic conversion, the calibration process and the range-migration calculation. The following extensions and changes have been made.

Data format

The raw data formats for Texas Instrument chips vary for most of their radar sensors. Thus the SAR-Toolbox was extended to work with the IWR6843 chip. This format is visualized in figure 5.10. The data reading and formatting was redesigned completely so that by configuring the sensor type, the software will automatically interpret the data correctly.

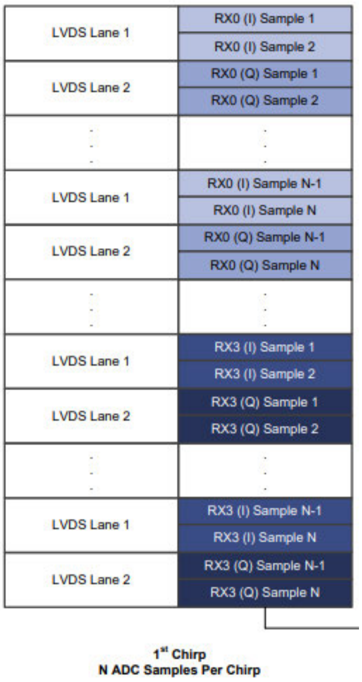

LVDS Lane 1	RX0 (I) Sample 1 RX0 (I) Sample 2
LVDS Lane 2	RX0 (Q) Sample 1 RX0 (Q) Sample 2
⋮	⋮
LVDS Lane 1	RX0 (I) Sample N-1 RX0 (I) Sample N
LVDS Lane 2	RX0 (Q) Sample N-1 RX0 (Q) Sample N
⋮	⋮
LVDS Lane 1	RX3 (I) Sample 1 RX3 (I) Sample 2
LVDS Lane 2	RX3 (Q) Sample 1 RX3 (Q) Sample 2
⋮	⋮
LVDS Lane 1	RX3 (I) Sample N-1 RX3 (I) Sample N
LVDS Lane 2	RX3 (Q) Sample N-1 RX3 (Q) Sample N

Figure 5.10: Complex data format for the IWR6843 radar sensor for one chirp recorded by 4 RX channels [75].

Antenna structure

Apart from being designed for 79 GHz radars, the antenna geometry is different from the IWR6843ISK and custom board geometry. The SAR-Toolbox was extended by the two geometries used in this work. Those definitions lay the basis for a correct multistatic to monostatic conversion. Extensions have also been made to the synthetic enlargement of the aperture as the custom board's virtual antenna array consists of 3 RX columns holding N samples for four antennas for every spatial sampling position, whereas the IWR6843ISK board only uses two TX antennas with N samples and omits the eccentric third element completely (compare to figure 5.7 and 5.4). Thus, the IWR6843ISK Matlab arrays will only consist of one RX column with N samples for eight rows.

Further changes

All parts of the software that were used, were adapted to 60 GHz operation and optimized or newly implemented to allow faster calculation with no frames and chirp repetitions used and movement in x-direction. To minimize calculation time, the averaging sections were removed as well as all upsampling procedures .

5.3 Measurement Procedure

The following section describes the measurement procedure by connecting the aforementioned components sequentially.

5.3.1 Device Configuration

The MMWave Studio API is used to connect all serial interfaces and Ethernet connections between PC and DCA1000EVM. After that the DCA1000EVM board and the respective radar sensor board is connected via SPI. The firmware for both the DSP and the MCU are flashed to the radar sensor. The data format and chirp configuration is transmitted and acknowledged. The radar sensor's RF interface is launched. After that, the stepper motor is connected via serial interface. When the first position reading is valid, the stepper is moved to its homing position.

5.3.2 Movement

The stepper motor is moved to the next sampling position. The position is read until it reaches the correct position with a tolerance of 0.03 mm. Upon reaching the position, the radar sensor is triggered via a software trigger and the capture process is launched on the DCA1000EVM board. While the board moves to the next position, the 16-bit binary data is transmitted to the PC and appended to the data structure. This parallel command processing allows to not only discreetly record radar data, but also continuously move the board and trigger the radar sensor upon reaching a predefined distance to the previous trigger location.

5.3.3 Post-processing

The data is processed after a certain number of measurements has been collected. This is currently the end of the rail, but could be adapted to continuously process N previous samples. This would allow for the robot it is attached to, to move inside a space of interest

Integrity check

The binary file is saved and has a size of

$$N_{Steps} \cdot N_{TX} \cdot N_{RX} \cdot 2(I\&Q) \cdot N_{Samples} \cdot 16 Bits \tag{5.1}$$

Data Input

The binary file is stored in the format presented in figure 5.10. After parsing the file with Matlab it is converted into a uniform array respective to the virtual antenna locations

Mono-static Conversion

The raw data is then converted from multistatic to monostatic, where each channel's TX - RX midpoint is set as a monostatic transceiver like described in 4.2.1. The physical antenna definition is defined for each board and can be extended for other configurations.

Calibration

The data is calibrated with the data recorded by the calibration procedure. This helps to compensate for phase mismatches induced by fabrication impurities and voltage offsets in the receiver structure.

Image Reproduction

The data is formed into a uniform array in y direction and, if possible in X-direction. This enables the application of the range-migration algorithm for discrete data. The interpolation in z-direction is performed to mitigate wave curvature effects. After that the multiplication of the decomposed k_z component with the two-dimensional Fourier transformation of the received data, the inverse three-dimensional Fourier transformation is performed. The result of this opertaion is a three-dimensional reflectivity matrix.

5.3.4 Calibration

Using a practical system inserts measurement errors into the setup which stem from differing sensor gain and phase mismatches [71]. These are caused by antenna feed-in points not being exactly equally distant from the chip's RF output, differences in the antennas or ICs themselves. These errors need to be compensated for by calibration.

[71]: Yanik (2020), 'Development and Demonstration of MIMO-SAR mmWave Imaging Testbeds'

5.4 Parameter Selection

This section details the parameters chosen for the verification of the methods with the implementation detailed above. The two board mainly differ in the SAR aperture they form based on their hardware specifications and the resulting possibilities for variations in the sampling distance and extent in Y-direction.

5.4.1 Sensor and Chirp Parameters

The chosen sensor parameters are specified in the Matlab measurement script and are sent to the DCA1000EVM board via the application programming interface of MMWave Studio.

Table 5.2: Selected parameters for the radar sensor configured in MMWave Studio.

Parameter	Value	Unit	Justification
Chirp start frequency	60	$10^9\ Hz$	Exploit the sensor bandwidth for maximum range resolution
Frequency slope	69.813	$10^{12}\ Hz \cdot s^{-1}$	Chosen based on the required sampling frequency
ADC Start Time	0.1	$10^{-6}\ s$	Seamless start of the ADC due to low amount of chirp repetitions
ADC Samples	256	-	Maximum number of samples to be sampled until ramp ends with the given sampling frequency
Sample Rate	4480	$10^3\ s^{-1}$	To reduce the range to the region of interest
Ramp End Time	57.26	$10^{-6}\ s$	ADC Start time + $N_{samples}/f_s$
Bandwidth	3.997	$10^9\ Hz$	Resulting from the ramp duration and the ramp slope
Number of chirp profiles	3	-	Three different chirp profiles with one of the three tranmitters turned on
Number of chirp loops	1	-	No chirp repetition to generate the minimum data
Number of frames	1	-	Not needed as the velocity FFT is not performed

5.4.2 SAR Parameters

The SAR parameters define the resulting synthetic aperture of the evaluation. The primarily varied parameters are the distance the system travels and the step size parameter. The important parameters are shown in table 5.3 for the IWR6843ISK board and in table 5.4 for the custom board.

Table 5.3: Selected parameters for the stepper motor and SAR setup for the IWR6843ISK board.

Parameter	Value	Unit	Justification
Sampling distance	Δx	m	Varies based on the used board and the requirement of a uniform array in x direction
Y aperture size	8.75	$10^{-3}\ m$	8 monostatic elements in y direction
X aperture size	X	m	Results from the amount of steps and the chosen sampling distance
Number of steps	N	-	Maximum number of steps based on the distance traveled by the stepper motor divided by the sampling distance

Table 5.4: Selected parameters for the stepper motor and SAR setup for the custom board.

Parameter	Value	Unit	Justification
Sampling distance	7.25	$10^{-3}\ m$	Fixed for the custom board to form a uniform array in x direction
Y aperture size	7.25	$10^{-3}\ m$	4 monostatic elements in y direction
X aperture size	X	m	Results from the amount of steps and the chosen sampling distance
Number of steps	N	-	Maximum number of steps based on the distance traveled by the stepper motor divided by the sampling distance

Results 6

The following section describes the results of multiple measurements taken to verify the methods proposed in chapter 4 with the implementation detailed in the previous chapter. Measurements where undertaken with both the publicly sold board by TI as well as the custom board featuring the IWR6843 chip.

6.1 IWR6843ISK Radar Board

6.1.1 Overhead Small Objects Evaluation

For the measurements in figure 6.2 and 6.1, the sampling distance was 2 mm with a resulting aperture size of 650 mm. With 8 virtual antennas in Y-direction and only one in X-direction, the resulting number of sampling positions was 325. The total aperture size is thus 325 x 8 virtual antennas. One setup was constructed to examine the spatial resolution and ability to detect concealed objects. A picture can be seen in figure 6.3. All objects can be observed in the reflectivity image both in X-Y slices (figure 6.2 and 6.1) and X-Z direction (figure 6.1). The expansion in X-direction is correct even though clean borders are not present due to blur. For the second setup a human arm was placed on approximately the same height as the cardboard box to evaluate the recognisability itself and distinguishability to metal objects. The human tissue has, as predicted in 3.2 a much lower reflection coefficient even though the area of reflection is much larger than that of the flange bushing which are downward facing.

The IWR6843ISK radar X-Z-slice shows all objects in the scene with correct range and spread in X-direction. The resolution in Y-direction suffers from the low size of the aperture. The flange bushings inside the cardboard box show a clearly visible radar reflection albeit scattered. The size in range direction is also correct in respect to the previously calculated range resolution.

6.1.2 Ground Level Evaluation

For this measurement the linear rail motor was placed approximately 200 mm above the ground. The aperture is fixed at a 90°

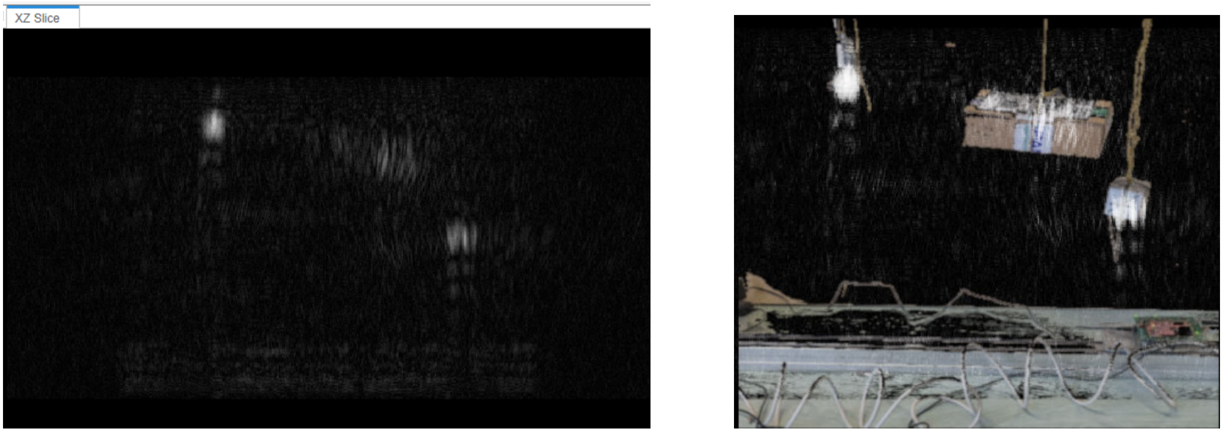

(a) **(b)**

Figure 6.1: X-Z slice of the scene. From left to right is the convex reflector, the concealed flange bushings and the aluminium cube. (b) shows an overlay of a photo of the actual scene with the objects at the correct positions.

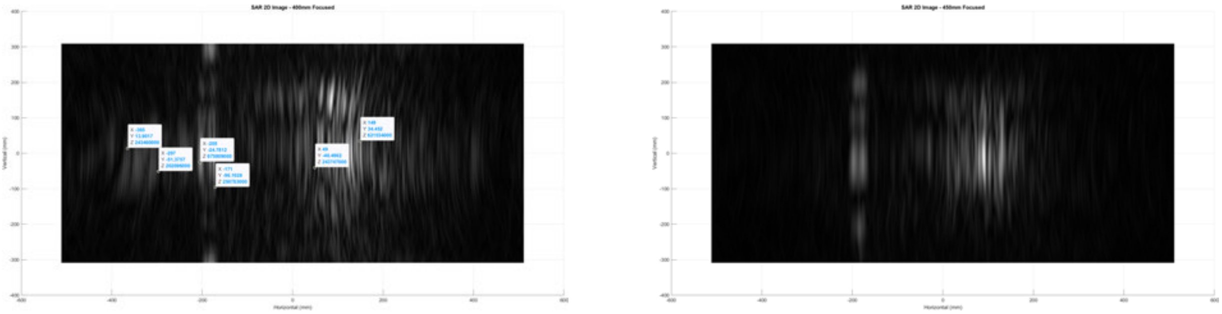

Figure 6.2: Sampling of the scene in figure 6.3. A human arm was added to the scene between the first two markers. It is visible with its correct extent in X-direction when focusing on the correct range. The arm is no longer visible on image (b) as it is focused 5 cm behind the arm. The flange bushings are still visible, the convex objects ghosts come into view because of its high reflectivity.

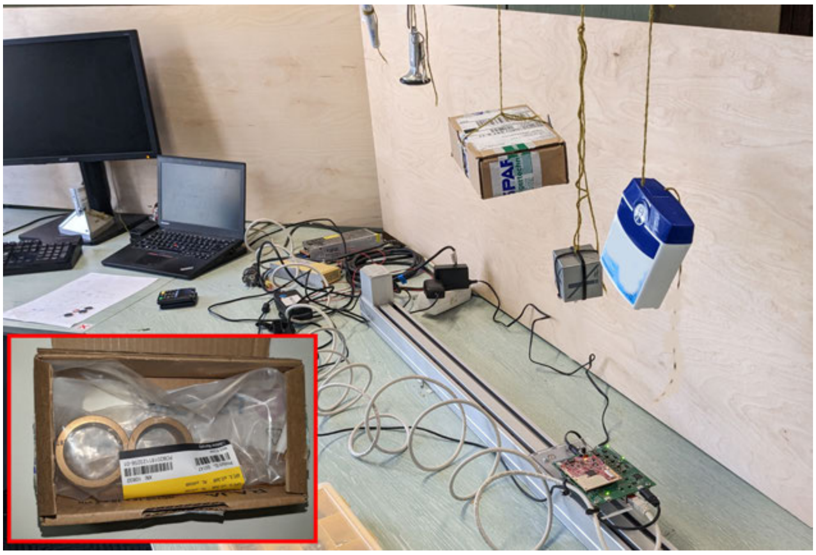

Figure 6.3: Picture of the spatial resolution test with two brass flange bushings concealed in a cardboard box.

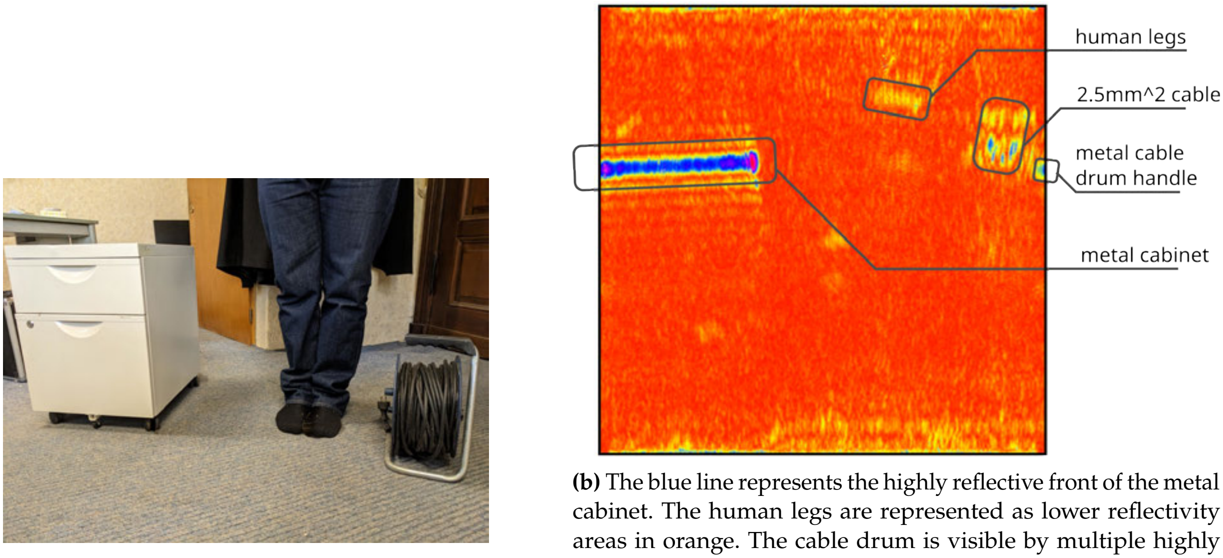

(a)

(b) The blue line represents the highly reflective front of the metal cabinet. The human legs are represented as lower reflectivity areas in orange. The cable drum is visible by multiple highly reflective dots.

Figure 6.4: The scene features a metal cabinet, a cable drum and a person. The sampled distance is 1000mm. The sampling step is 2.0 mm. All three objects are clearly visible with correct distance from the aperture and size. The metal objects are more reflective and are therefore differentiable to the human tissue. It is worth noting that their cross section is very low in case of the drum handle and cable.

angle respective to the floor. the sampling distance was set to 2 mm, the distance the motor travelled was 980 mm resulting in a total of 490 sampling positions. A human is present in front of the radar, a cable drum with 2.5 mm^2 cable, plastic drum and metal handle and a metal cabinet, placed with a slight angle, were added to the scene. The result shows only the X-Z slice of the result, the X-Y slice is equally blurry as the previous measurement.
The objects made from conductive materials are differentiable from the human tissue and bone. The human legs are clearly above the noise floor, though some ghosts targets with a similar footprint can be seen. The side wall of the cabinet can not be made out, this is due to the tilted front an the very narrow opening angle of the IWR6843ISK board. It is worth noting, that the metal cable drum handle is visible at that distance even tough is is only 17 mm in diameter. The limits for resolution in X-direction stated in section 3.3.2 of 9 mm for a opening angle of 60° are thereby confirmed.

The effects of varying the spatial sampling distance are evaluated in figure 6.5. The imaging system is at the same position as in the previous measurement. The scene consists of a plastic storage box made of 1 mm strong polypropylene plastic containing a calibration source with a metal casing. A metal cabinet is placed in the scene with a slight angle to the aperture. The sampling distance was varied from the maximum theoretical distance of 2.41 mm, half of the wavelength to 4 and 10 mm. The resulting apertures are

414 x 8, 250 x 8 and 100 x 8 with a total movement distance of 1000 mm. The previously documented correct spatial proportions, reflectivity distinctness and discoverability of conductive objects is validated. The predicted ghosts targets resulting from violations of the Nyquist theorem are visible in both pictures (see figure 6.5c and figure 6.5d). The violation of the sampling theorem in Z-direction due to the technical limitations of the fast chirp approach can be observed as attenuated copies of the physical structures in the X-Z-slice.

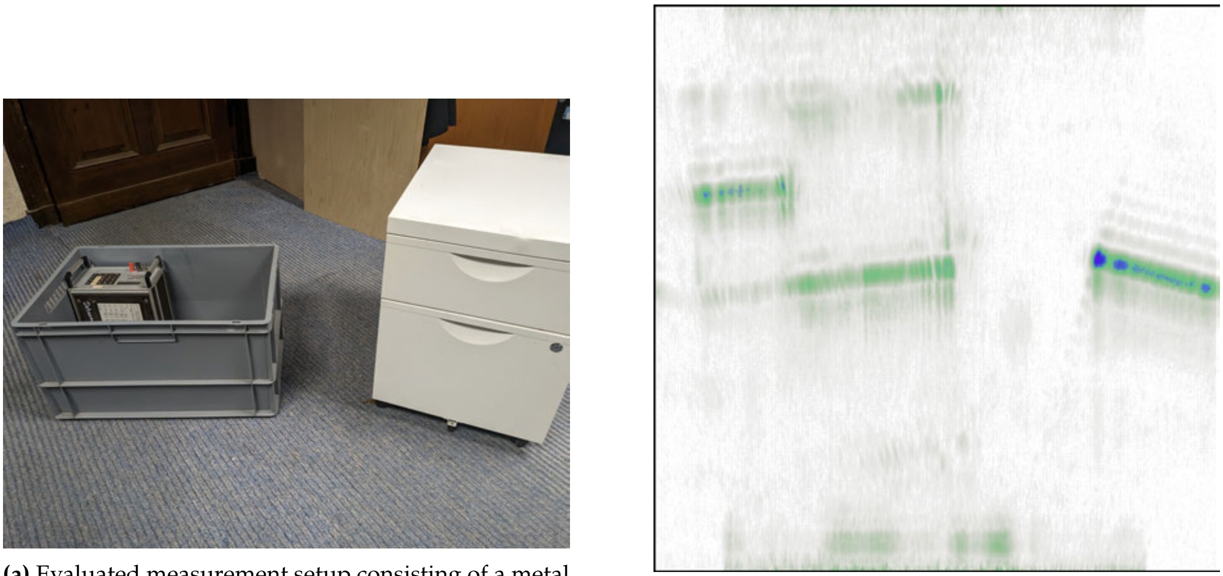

(a) Evaluated measurement setup consisting of a metal cabinet, a plastic storage box with a calibration source in a metal casing.

(b) Resulting maximum intensity projection for $\frac{\lambda}{2} = 2.41$ mm sampling distance.

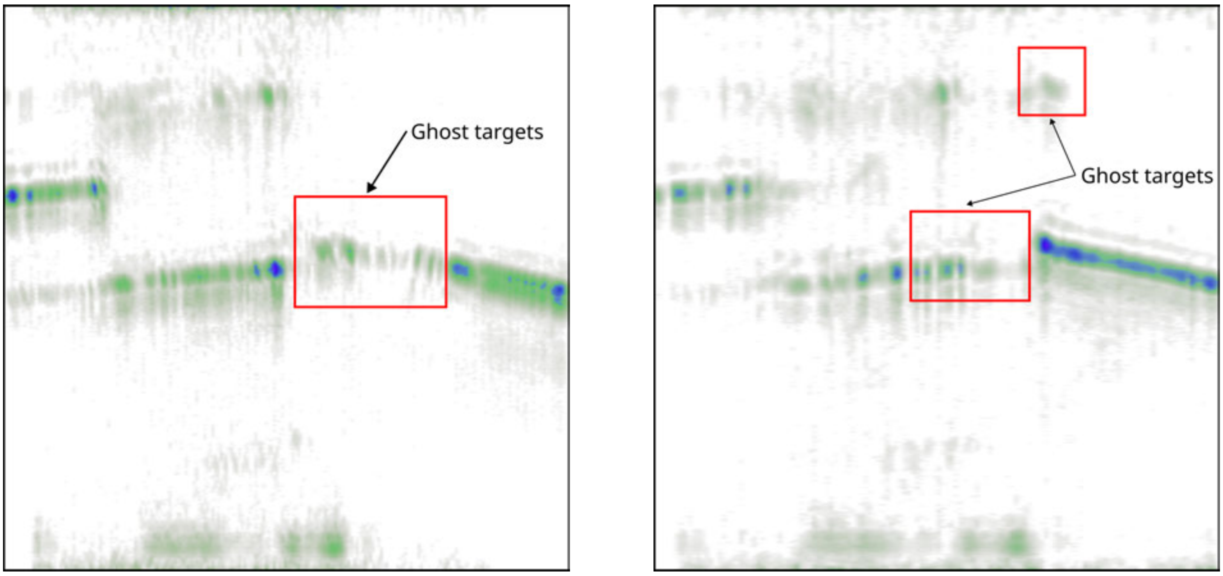

(c) Resulting maximum intensity projection for 4 mm sampling distance. Ghost targets appear between the two objects.

(d) Resulting maximum intensity projection for 10 mm sampling distance. More ghost targets appear. Spatial proportions start to diminish significantly.

Figure 6.5: The structures present in the scene are visible in their correct spatial dimensions. Metal objects have a noticeable difference in reflectivity even when behind cover. The attenuation in reflectivity of the plastic box is noteworthy. The two bottom measurements are taken with a sampling distance violating the $\frac{\lambda}{2}$ sampling distance. As predicted ghost targets start to appear resulting from range ambiguities in the range migration algorithm. Apart from this the resolution and correct spatial proportion start to diminish considerably.

6.2 IWR6843 Custom Board

The imaging results of the board can be observed in figure 6.6. As the board has an antenna extent in both X- and Y-direction and a virtual antenna array resulting in a 3 x 4 configuration (see fig. 5.7) the sampling distance is limited to the physical array antenna distances to form a uniform or equispaced array. The required step distance of the motor is therefore $\frac{3\lambda}{2}$. In total 90 recordings were done, resulting in a total aperture size of 650 mm. The antenna configuration's extent in Y-direction is only four transceiver elements compared to the 8 elements of the IWR6843ISK board. A total of 270 x 4 transceiver elements form the synthetic aperture. The placement of the items was identical to section 6.1, unfortunately none of the items are observable. A corner reflector was placed at 500 mm distance to evaluate the general functioning of the board. The de-chirped range FFT can be observed in 6.7. Although the picture shows only one TX channel, the results are nearly equivalent for all transmit channels. It can be observed, that the noise floor for all receivers varies by up to 20 dB. The same corner reflector was placed above the IWR6843ISK board at 800 mm. The results can be seen in figure 6.8. The noise floor is equally low on all receiver elements. Cross-talk can be observed as well, but is not higher than the reflection of the target itself.

The reason for the low quality of the picture is, that the noise floor varies greatly between the four channels, up to 20 dB. As the picture 6.6 shows a non-logarithmic 2D image plane, the varying signal strengths between the four channels result in the visible stripes. The distance between those stripes is exactly the distance between to virtual antenna phase centers. A large difference in the noise floor is detrimental, because the range migration algorithm evaluates the reflectivity at every point in space. If the actual objects

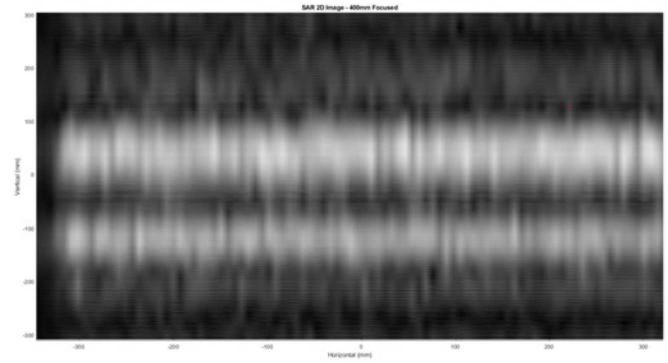

Figure 6.6: Reflectivity map at 400 mm distance. No objects present can be observed in the image. The images is dominated by strip structures in both the X-direction with a distance of 7.25 mm which is the sampling step distance as well as in the Y-direction.

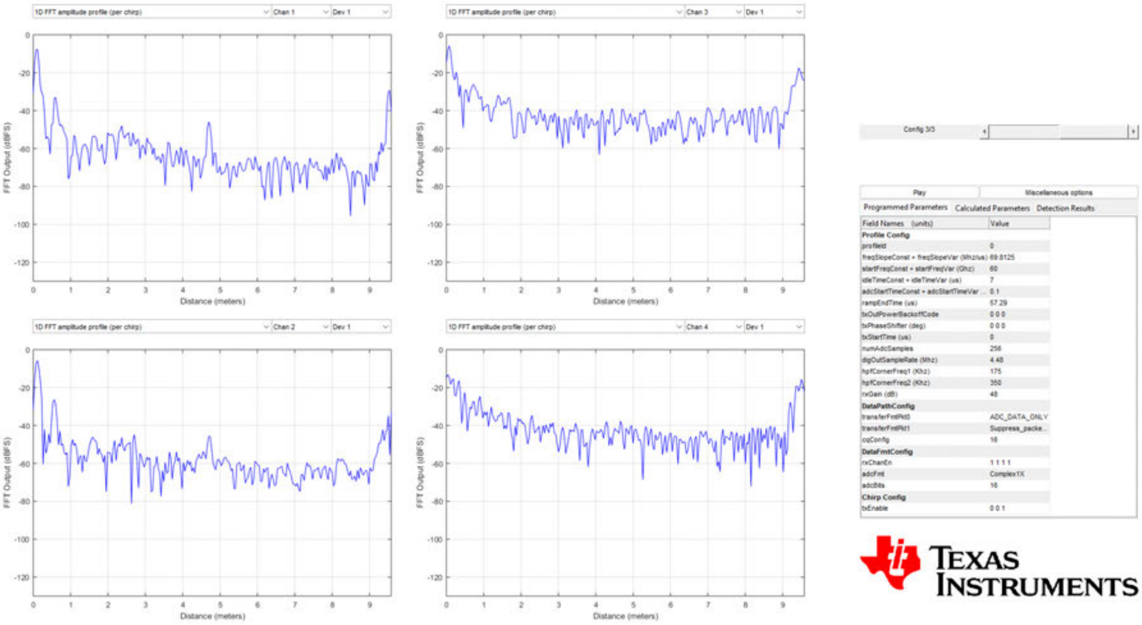

Field Names (units)	Value
Profile Config	
profileId	0
freqSlopeConst + freqSlopeVar (Mhz/us)	69.8125
startFreqConst + startFreqVar (Ghz)	60
idleTimeConst + idleTimeVar (us)	7
adcStartTimeConst + adcStartTimeVar ...	0.1
rampEndTime (us)	57.29
txOutPowerBackoffCode	0 0 0
txPhaseShifter (deg)	0 0 0
txStartTime (us)	0
numAdcSamples	256
digOutSampleRate (Mhz)	4.48
hpfCornerFreq1 (Khz)	175
hpfCornerFreq2 (Khz)	350
rxGain (dB)	48
DataPathConfig	
transferFmtPkt0	ADC_DATA_ONLY
transferFmtPkt1	Suppress_packe...
cqConfig	16
DataFmtConfig	
rxChanEn	1 1 1 1
adcFmt	Complex1X
adcBits	16
Chirp Config	
txEnable	0 0 1

Figure 6.7: Range FFT for the custom antenna board. Channel 1 to 4 from top to bottom and left to right. The third transmitter is switched on. A corner reflector was placed at 500 mm in front of the board. The noise floor varies by 20 dB between channels. The corner reflector can be barely seen on channel 3 and 4. The predominant direct cross talk is placed at 100 mm.

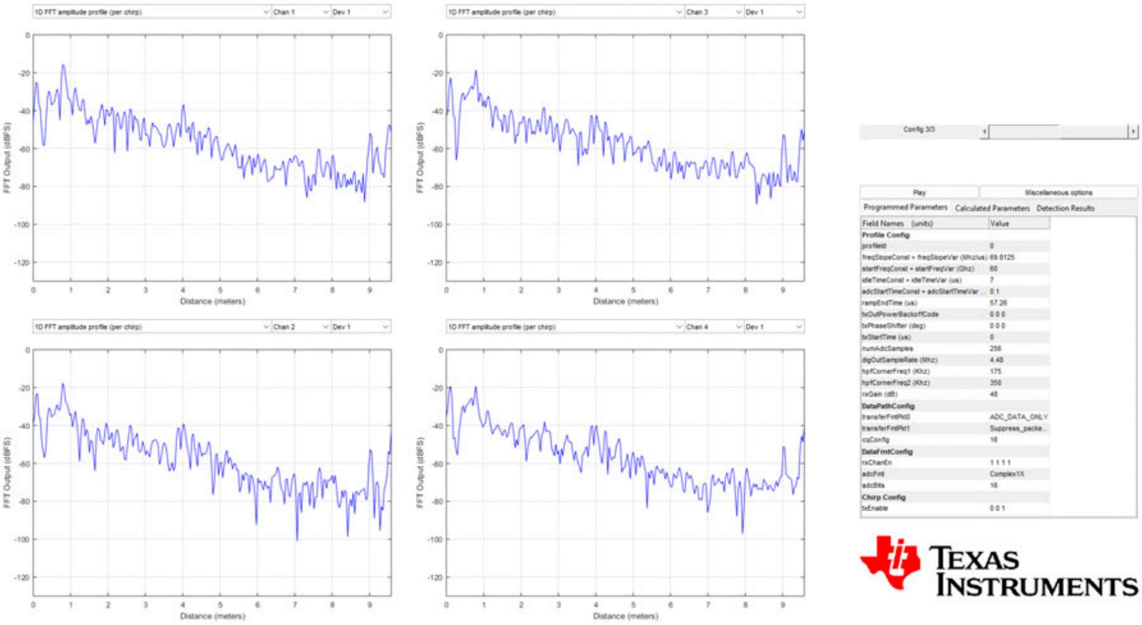

Field Names (units)	Value
Profile Config	
profileId	0
freqSlopeConst + freqSlopeVar (Mhz/us)	69.8125
startFreqConst + startFreqVar (Ghz)	60
idleTimeConst + idleTimeVar (us)	7
adcStartTimeConst + adcStartTimeVar ...	0.1
rampEndTime (us)	57.26
txOutPowerBackoffCode	0 0 0
txPhaseShifter (deg)	0 0 0
txStartTime (us)	0
numAdcSamples	256
digOutSampleRate (Mhz)	4.48
hpfCornerFreq1 (Khz)	175
hpfCornerFreq2 (Khz)	350
rxGain (dB)	48
DataPathConfig	
transferFmtPkt0	ADC_DATA_ONLY
transferFmtPkt1	Suppress_packe...
cqConfig	16
DataFmtConfig	
rxChanEn	1 1 1 1
adcFmt	Complex1X
adcBits	16
Chirp Config	
txEnable	0 0 1

Figure 6.8: The four channels of the ISK antenna board with transmitter number 3 switched on. The cross talk can be observed at 100 mm distance. The corner reflector is visible at 800 mm distance. The noise floor is consistent on all four receiving channels.

are not clearly separable from the noise itself, varying noise levels will be observable in the reflection map.

Other objects were tested, but metal corner reflector has the largest radar cross section in comparison. It barely stands out over the noise floor of the receiver. The only noticeable peak is a very close reflection which can be interpreted as direct radiation from the transmitter to the receiver. With a correct calibration this peak can be leveled out, by virtually shifting it behind the imaging aperture. This is a viable approach if the signal to noise ratio for objects in range, such as the corner reflector, is sufficient to detect them. A human arm or a plastic box are not detected at all on 3 out of 4 receivers.

The technical reason for the poor quality of the system lies in production faults: On the one hand, the top layer structures were partly filled with solder paste, on the other, the solder mask was not accurately applied. This lead to the antennas having a high amount of cross-talk combined with a poor radiation characteristic.

6.3 Discussion

While the non-uniform approach with the IWR6843ISK radar board shows usable results, the interpolation needs to be improved for varying movement speeds and stops of a robot. Forming an aperture under such conditions represents a very challenging task in regard of sampling implementations. The target system needs to be more clearly defined to continue this line of the research.

A varying Z-position of the antenna plane is not implemented. Research in that area is detailed in 2.3 but the robot movement procedures have to be clarified. If the robot moves on straight paths with the antenna fixed parallel to the movement direction, a varying z position is not needed. An implementation of fusing the radar images based on the rotation can be implemented similar to camera images and is not needed to be done in the range-migration algorithm. If the robot, in contrast, moves in other directions in respect to the antenna plane e.g. with omnidirectional wheels, an implementation of a 3D aperture is mandatory.

It was not evaluated how accurate a contemporary positioning system is, to be able to precisely track the sampling positions along a movement path. The data acquisition with the provided software was slow, so that it was appropriate to stop the sleigh altogether to record a chirp. Sampling continuously along a path is obviously the goal. For this reason, first steps to rewrite the data acquisition process were taken, but have not reached a stable state during this work and are not needed to evaluate the concept itself. Yanik et al. [71] points out errors introduced by sampling while moving. The conclusion of his work can be utilized to implement correct interpolation. The research of Smith et al. [51] can be used to implement three-dimensional arbitrary apertures.

[71]: Yanik (2020), 'Development and Demonstration of MIMO-SAR mmWave Imaging Testbeds'

[51]: Smith et al. (2022), 'Efficient 3-D Near-Field MIMO-SAR Imaging for Irregular Scanning Geometries'

It was both theoretically and practically evaluated in this work how the low size of an aperture in Y-direction affects the resolution. The aperture extend in this direction can not be synthetically enlarged without fundamentally changing the idea of an aperture being moved by a robot. It can thus be said that it is more important to physically enlarge the antenna array in this direction, if resolution in Y-direction is needed for the system. Enlarging the system in X-direction reduces the amount of sampling positions, but can be mitigated with improved ADC sweep slopes and sampling rates.

The angle of incident and the material are the basis for the recognition and imaging of the proposed system. Clear differentiability is shown with the focus on humans and conducting materials. An industrial setting also features various other materials which are not present in this work. The theoretical basis presented in 3.2 shows that reflectivity can not be taken as a single source of truth, but rather as an addition to other sensors. The density of sampling positions and the fast processing of the received data plays a key role, meaning that real time information about the reflectivity of encountered objects has to be gained. One key problem remains, which is, that in reality humans are not static objects but rather moving actors in the vicinity of a robot. Even if frame rate of the system is high by reducing the sampled distance until a new picture is formed, a SAR approach is unable to coherently image a moving target. This is especially the case for targets moving faster than the system. The effect can only be accounted for, if the physical aperture extent in movement direction and therefore the simultaneously captured space equals the imaged object in size.

Conclusion 7

In this work, methods are developed to integrate state of the art radar technology into the realm of robotic perception. Two different radar systems are compared in their capacity to differentiate between materials by their reflectivity. Their applicability for robot-robot and human-robot collaborative environments was evaluated in terms of gaining another vector of perception. A modern SAR imaging algorithm was used in combination with both widely available and cost-efficient evaluation hardware, as well as a custom MIMO array. All the hardware used is currently available on the market and economically approachable. A circuit board to attach custom radar boards to the TI DCA1000EVM was designed to easily interchange and test different radar sensors in the future. Existing open source radar imaging libraries were optimized for fast data acquisition and processing. They were also extended to support custom antenna layouts as well as 60 GHz TI radar sensors. With a practical development goal in mind, the groundwork for further development of a supplementary sensor solution was laid.

The capacity of the custom radar board could not be evaluated due to flaws in the production quality. The implementation of both the adapter board and the software components do not need further changes for a renewed assessment of the proposed setup. This is the first time the novel antenna layout was evaluated at all, and the research is therefore beneficial to the goal of improving the custom board to market readiness.

Finally, this research showed that MIMO-SAR using the range migration algorithm poses a valuable addition to robot perception. It was able to image hidden objects, differentiate between conducting materials and human tissue or other dielectrics. It opened an interesting field of research due to the sparse scientific coverage in recent years.

Practical applicability can be further verified by an evaluation with a clearly defined robotic system as well as an implementation of on-chip signal processing to reduce the bottlenecks imposed by the used evaluation software.

The limitations for the formulated goal of improving safety for human-robot collaborations were empirically laid out by this work: On the one hand, the SAR approach has shown, that the aperture needs to be equally large as the space it surveys. A large array in height is therefore needed to accurately image a human body. On the other hand, scenes moving faster than the robot itself will have low or no informational value. The overall practicality of specifically ensuring safe encounters between robots and humans is questionable. Nonetheless, the opportunities for various industrial application areas gained by using the described approach are manifold. They could be parcel inspection for warehouses, mapping of metallic structures such as shelves and production lines, pathfinding in areas with no ambient light or impaired visibility by smoke and dust. This could be especially useful for fire brigades and search and rescue operations.

Bibliography

Here are the references in citation order.

[1] International Federation of Robotics. *IFR Press Conference*. International Federation of Robotics. Sept. 24, 2020. URL: `https://ifr.org/downloads/press2018/Presentation WR 2020.pdf` (visited on 01/04/2023) (cited on page 1).

[2] Eric C. Dahlin. 'Are Robots Stealing Our Jobs?' In: *Socius Sociological Research for a Dynamic World* (May 2019), p. 15. DOI: `10.1177/2378023119846249` (cited on page 1).

[3] Zoltán Cséfalvay. 'As "robots are moving out of the cages" – toward a geography of robotization'. In: *Eurasian Geography and Economics* (Sept. 2021). DOI: `10.1080/15387216.2021.1972022` (cited on page 1).

[4] ISO. *Robots and robotic devices - Safety requirements for industrial robots - Part 2: Robot systems and integration*. Beuth Verlag, Berlin, 2012 (cited on page 1).

[5] Jeremy A. Marvel, Joe Falco, and Ilari Marstio. 'Characterizing Task-Based Human–Robot Collaboration Safety in Manufacturing'. In: *IEEE Transactions on Systems, Man, and Cybernetics: Systems* 45.2 (2015), pp. 260–275. DOI: `10.1109/TSMC.2014.2337275` (cited on page 1).

[6] P. Aivaliotis et al. 'Power and force limiting on industrial robots for human-robot collaboration'. In: *Robotics and Computer-Integrated Manufacturing* 59 (2019), pp. 346–360. DOI: `https://doi.org/10.1016/j.rcim.2019.05.001` (cited on page 1).

[7] Milos Vasic and Aude Billard. 'Safety Issues in Human-Robot Interactions'. In: *Institute of Electrical and Electronics Engineers (IEEE)* (Feb. 2013). DOI: `10.1109/ICRA.2013.6630576` (cited on page 1).

[8] Chien-Ming Huang and Bilge Mutlu. 'Anticipatory Robot Control for Efficient Human-Robot Collaboration'. In: *The Eleventh ACM/IEEE International Conference on Human Robot Interaction*. HRI '16. event-place: Christchurch, New Zealand. IEEE Press, 2016, pp. 83–90 (cited on page 1).

[9] Gaoyang Pang, Geng Yang, and Zhibo Pang. 'Review of Robot Skin: A Potential Enabler for Safe Collaboration, Immersive Teleoperation, and Affective Interaction of Future Collaborative Robots'. In: *IEEE Transactions on Medical Robotics and Bionics* 3.3 (Aug. 2021), pp. 681–700. DOI: `10.1109/TMRB.2021.3097252`. (Visited on 11/30/2022) (cited on page 2).

[10] Tin Lun Lam et al. 'Collision avoidance of industrial robot arms using an invisible sensitive skin'. In: *2012 IEEE/RSJ International Conference on Intelligent Robots and Systems*. Vilamoura-Algarve, Portugal: IEEE, Oct. 2012, pp. 4542–4543. DOI: `10.1109/IROS.2012.6386294`. (Visited on 11/30/2022) (cited on page 2).

[11] D.M. Ebert and D.D. Henrich. 'Safe human-robot-cooperation: image-based collision detection for industrial robots'. In: *IEEE/RSJ International Conference on Intelligent Robots and System*. Vol. 2. Lausanne, Switzerland: IEEE, 2002, pp. 1826–1831. DOI: `10.1109/IRDS.2002.1044021`. (Visited on 11/30/2022) (cited on page 2).

[12] Tapio Taipalus and Juhana Ahtiainen. ‘Human detection and tracking with knee-high mobile 2D LIDAR’. In: *2011 IEEE International Conference on Robotics and Biomimetics*. Karon Beach, Thailand: IEEE, Dec. 2011, pp. 1672–1677. DOI: `10.1109/ROBIO.2011.6181529`. (Visited on 11/30/2022) (cited on page 2).

[13] Rammeter. *flir si124 industrial ultrasound imaging cameras*. English. URL: `https://www.rammeter.com/flir-si124-industrial-ultrasound-imaging-camera` (visited on 03/01/2023) (cited on page 3).

[14] Kim Mathiassen et al. ‘An Ultrasound Robotic System Using the Commercial Robot UR5’. In: *Frontiers in Robotics and AI* 3 (2016). DOI: `10.3389/frobt.2016.00001` (cited on page 3).

[15] Matthias Scheutz, John McRaven, and Gyorgy Cserey. ‘Fast, reliable, adaptive, bimodal people tracking for indoor environments’. In: *2004 IEEE/RSJ International Conference on Intelligent Robots and Systems, Sendai, Japan, September 28 - October 2, 2004*. IEEE, 2004, pp. 1347–1352. DOI: `10.1109/IROS.2004.1389583` (cited on page 3).

[16] Kai O. Arras, Oscar Martinez Mozos, and Wolfram Burgard. ‘Using Boosted Features for the Detection of People in 2D Range Data’. In: *Proceedings 2007 IEEE International Conference on Robotics and Automation*. 2007, pp. 3402–3407. DOI: `10.1109/ROBOT.2007.363998` (cited on page 3).

[17] Peter Chemweno and Robbert-Jan Torn. ‘Innovative safety zoning for collaborative robots utilizing Kinect and LiDAR sensory approaches’. In: *Procedia CIRP* 106 (2022). 9th CIRP Conference on Assembly Technology and Systems, pp. 209–214. DOI: `https://doi.org/10.1016/j.procir.2022.02.180` (cited on page 3).

[18] Merrill I.. Skolnik. ‘radar’. In: *Encyclopedia Britannica*. Sept. 2022. (Visited on 01/12/2022) (cited on page 4).

[19] Aaron Kline. *AIS vs Radar: Vessel Tracking Options*. English. News. July 2018. URL: `https://web.archive.org/web/20190202042639/https://www.portvision.com/news-events/press-releases-news/ais-vs-radar-vessel-tracking-optionsportvision` (visited on 01/12/2022) (cited on page 4).

[20] Akram Al-Hourani et al. ‘Millimeter-wave integrated radar systems and techniques’. en. In: *Academic Press Library in Signal Processing, Volume 7*. Elsevier, 2018, pp. 317–363. DOI: `10.1016/B978-0-12-811887-0.00007-9`. (Visited on 12/01/2022) (cited on page 4).

[21] Cesar Iovescu and Rao Sandeep. *The fundamentals of millimeter wave radar sensors*. English. July 2020. URL: `https://www.ti.com/lit/wp/spyy005a/spyy005a.pdf?ts=1669880420604&ref url=https%253A%252F%252Fwww.google.com%252F` (visited on 01/12/2022) (cited on page 4).

[22] Mingchang Zhao, Abdelhamid Mammeri, and Azzedine Boukerche. ‘Distance measurement system for smart vehicles’. In: *2015 7th International Conference on New Technologies, Mobility and Security (NTMS)*. Paris, France: IEEE, July 2015, pp. 1–5. DOI: `10.1109/NTMS.2015.7266486`. (Visited on 12/01/2022) (cited on page 4).

[23] Jürgen Hasch et al. ‘Millimeter-Wave Technology for Automotive Radar Sensors in the 77 GHz Frequency Band’. In: *IEEE Transactions on Microwave Theory and Techniques* 60.3 (Mar. 2012), pp. 845–860. doi: 10.1109/TMTT.2011.2178427. (Visited on 11/30/2022) (cited on page 4).

[24] ‘IEEE Standard Radar Definitions’. In: *IEEE Std 686-2008 (Revision of IEEE Std 686-1997)* (2008), pp. 1–44. doi: 10.1109/IEEESTD.2008.4530766 (cited on page 7).

[25] Sinan Kurt, Ş Demir, and Altunkan Hizal. ‘Zero crossing counter for accuracy improvement of FMCW range detection’. In: *Turkish Journal of Electrical Engineering and Computer Sciences* 16 (July 2008), pp. 125–132 (cited on page 7).

[26] Han Gil Choi, Sang Heung Lee, and Seong Hwan Cho. ‘Technique for fast triangular chirp modulation in FMCW PLL’. In: *IEICE Electronics Express* 19.14 (2022), pp. 20220214–20220214. doi: 10.1587/elex.19.20220214 (cited on page 7).

[27] Ziqiang Tong, Ralf Renter, and Masahiko Fujimoto. ‘Fast chirp FMCW radar in automotive applications’. In: *IET International Radar Conference 2015*. 2015, pp. 1–4. doi: 10.1049/cp.2015.1362 (cited on page 7).

[28] *IWR1642 Single-Chip 76- to 81-GHz mmWave Sensor*. SWRS212B. Rev. C. Texas Instruments. Apr. 2018 (cited on pages 8, 9).

[29] infineon. *XENSIV™ – sensing the world*. English. infineon, Nov. 2022. url: https://www.infineon.com/dgdl/Infineon-xensiv sensor solutions-ProductSelectionGuide-v01 00-EN.pdf (visited on 02/21/2022) (cited on page 8).

[30] Andrew Robertson, Maik Brett, and Ralf Reuter. *Increasing Automotive Safety Through Embedded Radar Technologies*. English. freescale, Nov. 2014. url: https://www.nxp.com/docs/en/white-paper/ADASRADARWP.pdf (visited on 02/20/2022) (cited on page 8).

[31] Anand Kumar et al. *A Compact Quasi-Yagi Antenna for FMCW Radar-on-Chip based Through-Wall Imaging*. 2022. doi: 10.48550/ARXIV.2208.11034. url: https://arxiv.org/abs/2208.11034 (cited on page 8).

[32] Adriano Meta, Peter Hoogeboom, and Leo P. Ligthart. ‘Signal Processing for FMCW SAR’. In: *IEEE Transactions on Geoscience and Remote Sensing* 45.11 (2007), pp. 3519–3532. doi: 10.1109/TGRS.2007.906140 (cited on page 9).

[33] *DCA1000EVM Data Capture Card*. SPRUIJ4A. Rev. A. Texas Instruments. May 2018 (cited on page 9).

[34] Jian Li and Petre Stoica. *MIMO radar signal processing*. English. John Wiley & Sons, Inc., Hoboken, New Jersey, 2009 (cited on page 11).

[35] Qian He, Yang Yang, and Rick S. Blum. ‘Chapter 13 - MIMO Radar with Widely Separated Antennas—From Concepts to Designs’. In: *Academic Press Library in Signal Processing: Volume 2*. Ed. by Nicholas D. Sidiropoulos et al. Vol. 2. Academic Press Library in Signal Processing. Elsevier, 2014, pp. 667–727. doi: https://doi.org/10.1016/B978-0-12-396500-4.00013-2 (cited on page 11).

[36] S. Sruti, Chilaka Deepti, and K. Giridhar. 'Non-Parametric and Geometric Multi-Target Data Association for Distributed MIMO Radars'. In: *MILCOM 2021 - 2021 IEEE Military Communications Conference (MILCOM)*. 2021, pp. 601–606. DOI: `10.1109/MILCOM52596.2021.9652943` (cited on page 11).

[37] Scott L. Cassidy et al. 'High resolution automotive imaging using MIMO radar and Doppler beam sharpening'. In: *IEEE Transactions on Aerospace and Electronic Systems* (2022), pp. 1–11. DOI: `10.1109/TAES.2022.3203953` (cited on page 11).

[38] Igal Bilik et al. 'Automotive MIMO radar for urban environments'. In: *2016 IEEE Radar Conference (RadarConf)*. 2016, pp. 1–6. DOI: `10.1109/RADAR.2016.7485215` (cited on page 11).

[39] Muhamed Rias. 'Direction of arrival using antenna arrays'. Jan. 1996. (Visited on 11/30/2022) (cited on page 12).

[40] Martin Kirscht and Carsten Rinke. '3D Reconstruction of Buildings and Vegetation from Synthetic Aperture Radar (SAR) Images'. In: *IAPR International Workshop on Machine Vision Applications*. 1998 (cited on page 12).

[41] Mohammed D. Buhari, Gui Yun Tian, and Rajesh Tiwari. 'Microwave-Based SAR Technique for Pipeline Inspection Using Autofocus Range-Doppler Algorithm'. In: *IEEE Sensors Journal* 19.5 (2019), pp. 1777–1787. DOI: `10.1109/JSEN.2018.2879348` (cited on page 12).

[42] Muhammet Emin Yanik and Murat Torlak. 'Near-Field 2-D SAR Imaging by Millimeter-Wave Radar for Concealed Item Detection'. In: *2019 IEEE Radio and Wireless Symposium (RWS)*. 2019, pp. 1–4. DOI: `10.1109/RWS.2019.8714552` (cited on page 12).

[43] Carmine Clemente and John J. Soraghan. 'Fractional Range Doppler Algorithm for SAR imaging'. In: *The 7th European Radar Conference*. 2010, pp. 248–251 (cited on page 13).

[44] Gregory L. Charvat, Alan J. Fenn, and Bradley T. Perry. 'The MIT IAP radar course: Build a small radar system capable of sensing range, Doppler, and synthetic aperture (SAR) imaging'. In: *2012 IEEE Radar Conference*. 2012, pp. 0138–0144. DOI: `10.1109/RADAR.2012.6212126` (cited on page 13).

[45] A.L. Boyer et al. 'Reconstruction of Ultrasonic Images by Backward Propagation'. In: *Acoustical Holography*. Vol. 3. IBM Scientific Center. Springer, 1971, pp. 248–251 (cited on page 13).

[46] D.M. Sheen, D.L. McMakin, and T.E. Hall. 'Three-dimensional millimeter-wave imaging for concealed weapon detection'. In: *IEEE Transactions on Microwave Theory and Techniques* 49.9 (2001), pp. 1581–1592. DOI: `10.1109/22.942570` (cited on pages 13, 19–21).

[47] Muhammet Emin Yanik. 'MILLIMETER-WAVE IMAGING USING MIMO-SAR TECHNIQUES'. In: *Dissertation* (Jan. 5, 2020), p. 173 (cited on page 13).

[48] Jingkun Gao et al. 'Novel Efficient 3D Short-Range Imaging Algorithms for a Scanning 1D-MIMO Array'. In: *IEEE Transactions on Image Processing* 27.7 (2018), pp. 3631–3643. DOI: `10.1109/TIP.2018.2821925` (cited on page 13).

[49] Aining Li. 'Algoritthms For The Implementation Of STOLT Interpolation In SAR Processing'. In: *[Proceedings] IGARSS '92 International Geoscience and Remote Sensing Symposium*. Vol. 1. 1992, pp. 360–362. DOI: `10.1109/IGARSS.1992.576711` (cited on page 13).

[50] Jianping Wang, Pascal Aubry, and Alexander Yarovoy. '3-D Short-Range Imaging With Irregular MIMO Arrays Using NUFFT-Based Range Migration Algorithm'. In: *IEEE Transactions on Geoscience and Remote Sensing* 58.7 (2020), pp. 4730–4742. DOI: `10.1109/TGRS.2020.2966368` (cited on page 13).

[51] Josiah W. Smith and Murat Torlak. 'Efficient 3-D Near-Field MIMO-SAR Imaging for Irregular Scanning Geometries'. In: *IEEE Access* 10 (2022), pp. 10283–10294. DOI: `10.1109/ACCESS.2022.3145370` (cited on pages 13, 57).

[52] Claire M. Watts et al. '2D and 3D millimeter-wave synthetic aperture radar imaging on a PR2 platform'. In: *2016 IEEE/RSJ International Conference on Intelligent Robots and Systems (IROS)*. 2016, pp. 4304–4310. DOI: `10.1109/IROS.2016.7759633` (cited on page 13).

[53] Tobias D. Carrigan et al. 'Nondestructive Testing of Nonmetallic Pipelines Using Microwave Reflectometry on an In-Line Inspection Robot'. In: *IEEE Transactions on Instrumentation and Measurement* 68.2 (2019), pp. 586–594. DOI: `10.1109/TIM.2018.2847780` (cited on page 13).

[54] Faiza Ali, Georg Bauer, and Martin Vossiek. 'A Rotating Synthetic Aperture Radar Imaging Concept for Robot Navigation'. In: *IEEE Transactions on Microwave Theory and Techniques* 62.7 (2014), pp. 1545–1553. DOI: `10.1109/TMTT.2014.2323013` (cited on page 13).

[55] Behzad Yektakhah, Kamal Sarabandi, and Hussein Nasser Shaman. 'High Resolution Subsurface 3D SAR Imaging Using Robotic Bi-Static Transceivers'. In: *2019 IEEE International Symposium on Antennas and Propagation and USNC-URSI Radio Science Meeting*. 2019, pp. 825–826. DOI: `10.1109/APUSNCURSINRSM.2019.8888534` (cited on page 14).

[56] Rebecca M. Williams, Laura E. Ray, and James H. Lever. 'Autonomous robotic ground penetrating radar surveys of ice sheets; Using machine learning to identify hidden crevasses'. In: *2012 IEEE International Conference on Imaging Systems and Techniques Proceedings*. 2012, pp. 7–12. DOI: `10.1109/IST.2012.6295593` (cited on page 14).

[57] Chang Cai et al. 'A Multi-Robot Coverage Path Planning Method for Maritime Search and Rescue Using Multiple AUVs'. In: *Remote Sensing* 15.1 (2023). DOI: `10.3390/rs15010093` (cited on page 14).

[58] Theodore S. Rappaport. *Wireless Communications - Principles and Practice*. Prentice Hall PTR, 2002 (cited on page 17).

[59] E. C. Jordan and K. G. Balmain. *Electromagnetic waves and radiating systems*. 2d ed. Englewood Cliffs, N.J.: Prentice-Hall, 1968 (cited on page 17).

[60] Paul R. Clayton. *Introduction to Electromagnetic Compatibility*. Hoboken, New Jersey: John Wiley & Sons, Inc., 2006 (cited on page 17).

[61] Ting Wu, T.S. Rappaport, and Christopher Collins. 'Safe for Generations to Come: Considerations of Safety for Millimeter Waves in Wireless Communications'. In: *IEEE Microwave Magazine* 16 (Mar. 2015), pp. 65–84. DOI: `10.1109/MMM.2014.2377587` (cited on page 19).

[62] Xiaodong Zhuge and Alexander G. Yarovoy. 'A Sparse Aperture MIMO-SAR-Based UWB Imaging System for Concealed Weapon Detection'. In: *IEEE Transactions on Geoscience and Remote Sensing* 49.1 (2011), pp. 509–518. DOI: `10.1109/TGRS.2010.2053038` (cited on page 19).

[63] Bernard D. Steinberg. ‘Principles of aperture and array system design: Including random and adaptive arrays’. In: 1976 (cited on page 21).

[64] Sandeep Rao. *Introduction to mmwave Sensing: FMCW Radars*. English. Texas Instruments, 2017. URL: `https://training.ti.com/sites/default/files/docs/mmwaveSensing-FMCW-offlineviewing 0.pdf` (visited on 01/12/2022) (cited on page 21).

[65] *MiR1350 - The most powerful AMR from MiR to date*. English. Mobile Industrial Robots. URL: `https://www.mobile-industrial-robots.com/solutions/robots/mir1350/` (visited on 03/01/2023) (cited on page 22).

[66] Nipper. *The compact automated guided vehicle system for pallet transport*. English. URL: `https://www.mobile-robots.de/100/autonomous-pallet-transport-amr-agv/nipper-pallet-truck` (visited on 03/01/2023) (cited on page 22).

[67] Innok Robotics. *Induros - Your superior AMR solution for intralogistics and logistics*. English. URL: `https://www.innok-robotics.de/produkte/induros/?gclid=EAIaIQobChMIv8H-1M66 QIV74xoCR2-RAK-EAAYAiAAEgIyMvD BwE` (visited on 03/01/2023) (cited on page 22).

[68] Jri Lee et al. ‘A Fully-Integrated 77-GHz FMCW Radar Transceiver in 65-nm CMOS Technology’. In: *IEEE Journal of Solid-State Circuits* 45.12 (2010), pp. 2746–2756. DOI: `10.1109/JSSC.2010.2075250` (cited on page 23).

[69] Ralph Jacobi and Artem Aginskiy. ‘Choosing 60-GHz mmWave sensors over 24-GHz to enable smarter industrial applications’. In: (2018) (cited on page 26).

[70] Joachim H. G. Ender and Jens Klare. ‘System architectures and algorithms for radar imaging by MIMO-SAR’. In: *2009 IEEE Radar Conference*. Pasadena, CA, USA: IEEE, 2009, pp. 1–6. DOI: `10.1109/RADAR.2009.4976997`. (Visited on 12/08/2022) (cited on page 27).

[71] Muhammet Emin Yanik. ‘Development and Demonstration of MIMO-SAR mmWave Imaging Testbeds’. In: *IEEE* (Apr. 7, 2020), p. 20 (cited on pages 28, 46, 57).

[72] *3D Wave Equation and Plane Waves / 3D Differential Operators*. English. Rammeter, Feb. 2013. URL: `http://www.physics.usu.edu/riffe/3750/Lecture%5C%2018.pdf` (visited on 03/03/2023) (cited on page 31).

[73] Boon Poh Ng et al. ‘A Practical Simple Geometry and Gain/Phase Calibration Technique for Antenna Array Processing’. In: *IEEE Transactions on Antennas and Propagation* 57.7 (2009), pp. 1963–1972. DOI: `10.1109/TAP.2009.2021931` (cited on page 33).

[74] C.M. Schmid et al. ‘An FMCW MIMO radar calibration and mutual coupling compensation approach’. In: Jan. 2013, pp. 13–16 (cited on page 33).

[75] *Mmwave Radar Device ADC Raw Data Captur*. SWRA581B. Rev. A. Texas Instruments. May 2018 (cited on page 44).

Special Terms

A

ADC Analog Digital Converter. 26, 35, 43

ASCII American Standard Code for Information Interchange. 41

C

CFAR Constant False Alarm Rate. 35

CMOS Complementary Metal-Oxide-Semiconductor. 11

COM Communication. 35

D

DIP Dual Input Package. 36

DSP Digital signal processor. viii, 11, 35, 37, 44

E

ETSI European Telecommunication Standards Institute. 25

F

FCC Federal Communications Commission. 25

FFT Fast Fourier Transformation. 9, 13, 35, 47, 54

FMCW Frequency-Modulated Continuous Wave. 7, 35, 43

FPGA Field Programmable Gate Array. viii, 35–37

FTDI Future Technology Devices International. 35

I

IC Integrated Circuit. 26, 35

IEEE Institute of Electrical and Electronics Engineers. 7

IF Intermediate Frequency. 9, 35

IZM Institut für Zuverlässigkeit und Mikrointegration. 35

L

LIDAR Light Detection and Ranging. 3, 4, 7

LVDS Low Voltage Differential Signal. viii, 35, 37, 43

M

MCU Micro Controller Unit. viii, 35, 37, 44

MIMO Multiple Input Multiple Output. 11–14, 19, 25

R

RCS Radar Cross Section. 11

S

SAR Synthetic Aperture Radar. 12–14, 19

SISO Single Input Single Output. 11, 13
SNR Signal-to-Noise Ratio. 7
SPI Serial Periphal Interface. 44

U

UART Universal Asynchronous Receiver Transmitter. 35, 40, 41
USB Universal Serial Bus. 35, 40

Erklärung zur selbstständigen Bearbeitung einer Abschlussarbeit

Hiermit versichere ich, dass ich die vorliegende Arbeit ohne fremde Hilfe selbständig verfasst und nur die angegebenen Hilfsmittel benutzt habe.

[redacted]

Berlin, den ________________